



OPEN ACCESS

EDITED BY

Yi Zheng,
Sun Yat-sen University, China

REVIEWED BY

Pura Alfonso,
Universitat Politècnica de Catalunya, Spain
Pei Ni,
Nanjing University, China

*CORRESPONDENCE

Valery Fridovsky,
✉ fridovsky@diamond.ysn.ru

RECEIVED 17 November 2023

ACCEPTED 19 January 2024

PUBLISHED 16 February 2024

CITATION

Fridovsky V, Kryazhev S, Polufuntikova L,
Kudrin M and Anisimova G (2024), Geology,
fluid inclusions, mineral and (S-O) isotope
chemistry of the Badran orogenic Au deposit,
Yana-Kolyma belt, eastern Siberia:
implications for ore genesis.
Front. Earth Sci. 12:1340112.
doi: 10.3389/feart.2024.1340112

COPYRIGHT

© 2024 Fridovsky, Kryazhev, Polufuntikova,
Kudrin and Anisimova. This is an open-access
article distributed under the terms of the
[Creative Commons Attribution License \(CC BY\)](https://creativecommons.org/licenses/by/4.0/). The use, distribution or reproduction in
other forums is permitted, provided the
original author(s) and the copyright owner(s)
are credited and that the original publication
in this journal is cited, in accordance with
accepted academic practice. No use,
distribution or reproduction is permitted
which does not comply with these terms.

Geology, fluid inclusions, mineral and (S-O) isotope chemistry of the Badran orogenic Au deposit, Yana-Kolyma belt, eastern Siberia: implications for ore genesis

Valery Fridovsky^{1*}, Sergey Kryazhev^{2,1}, Lena Polufuntikova¹, Maxim Kudrin¹ and Galina Anisimova¹

¹Diamond and Precious Metal Geology Institute, Siberian Branch of the Russian Academy of Sciences, Yakutsk, Russia, ²Central Research Institute of Geological Prospecting for Base and Precious Metals, Moscow, Russia

The Badran orogenic gold deposit is located in the Yana-Kolyma belt, Eastern Siberia; it has proven reserves of ~9.3 t of gold and an average grade of 7.8 ppm. The total gold production at the Badran deposit since 1984 amounts to ~34 t. Despite many years of study, the origin of the gold deposits of the Yana-Kolyma metallogenic belt, one of the world's largest belts, and the Badran deposit is controversial. Synthesis of regional geology and geology of the Badran deposit, fluid inclusion analysis, mineral and (S-O) isotope chemistry defines the genetic model, origin of fluids, and source of metals in the evolution of the ore-forming system, equivalent to other orogenic gold deposits on the margin of the Siberian craton. The deposit is localized in the Upper Triassic clastic rocks and is controlled by the NW-trending thrust. Polyphase mineralization occurs as disseminated arsenian pyrite and arsenopyrite ores with invisible gold, quartz veins with native gold and Fe, Pb, Zn, Cu sulfides and sulfosalts of orogenic type, and locally post-ore Ag, Sb-bearing minerals and Hg epithermal features. The quartz veins with native gold were formed from low-medium saline (1.5–10 wt% NaCl eq.) aqueous-carbonic fluids boiling at temperatures of 290°C to 210 °C and pressures of 300–250 to 125 bar. The $\delta^{34}\text{S}$ values of pyrite and arsenopyrite vary from -1.1‰ to +2.4‰, with an average of +0.4‰; the $\delta^{18}\text{O}$ of quartz from +15.1‰ to +17.5‰ at constant $\delta^{18}\text{O}_{\text{H}_2\text{O}}$ about +7.5‰ ($\pm 1.0\%$). High contents of As (up to 2.4 wt%) and Co/Ni ~ from 0.3 to 9.9 in pyrite of proximal alteration are typical for hydrothermal systems. The results obtained confirm that the ore-forming fluids did not have a single origin, but were formed from a mixture of subcontinental lithospheric mantle and metamorphic sources. The subcrustal lithospheric mantle was fertilized in the time preceding mineralization (Late Jurassic) and was derived directly from the down-going subduction slab and overlying sediment wedge at the closure of the Oymyakon Ocean.

KEYWORDS

geology, mineral, (S-O) isotope, Badran gold deposit, eastern Siberia

1 Introduction

On the regional scale, the Badran gold deposit is located in the rear of the Verkhoyansk fold-and-thrust belt southeast of the Yana-Kolyma orogenic belt (Figure 1). It belongs to the orogenic-type deposits characteristic of one of the world's largest Late Jurassic–Early Neocomian Yana-Kolyma metallogenic belts, where the total amount of gold produced and recorded in resources is ~8320 tons (Goryachev and Pirajno, 2014). Here, along with large orogenic gold deposits (Natalka, Degdekan, Pavlik, Drazhnoe, and others), intrusion-related Au deposits of smaller size are also known (Chepak, Teutedjak, Chistoe, Ergelyakh, and others), along with related Quaternary placers (Fridovsky, 2002; Goldfarb et al., 2014; Goryachev and Pirajno, 2014; Fridovsky, 2018; Vikent'eva et al., 2018). There are also Au-Sb, Mo-W, and Sn-W deposits in this territory (Figure 1).

The Badran deposit was discovered in 1961, explored in 1970–1980, and in 1956–1976 by trenching and drilling, and underground mining. In 1984 underground Au mining began at the field, which continues to the present day. The total volume of gold production is about 34 tons. The gold reserves of the deposit are estimated at ~9.3 t with an average content of 7.8 ppm. The deposit has been explored by surface and underground workings at a distance of more than 5 km; a downdip of more than 1.2 km makes it possible to study the structure of the deposit, the mineral composition of ores and the conditions of ore formation at various deep levels. The results of studying various aspects of geology, mineralogy, and conditions of ore formation of the Badran deposit are considered in a number of scientific papers (Anisimova et al., 1998; Fridovsky, 1999; Fridovsky, 2002; Fridovsky, 2018; Neustroev, 2003; Amuzinsky, 2005; Anisimova et al., 2008; Konstantinov, 2010; Obolensky et al., 2011).

Despite many years of study, the origin of the gold deposits of the Yana-Kolyma metallogenic belt and the Badran deposit is controversial. Based on the example of a large Natalka deposit, water entry from a magmatic source is proven (Goryachev et al., 2008). Gamyanin et al. (2018) explain the formation of the OGD region by the involvement of metamorphic fluids. A study by Obolensky et al. (2011) suggested that the Badran deposit was formed during the evolution of a metamorphic hydrothermal system with an important contribution to mantle fluids. For this reason, the main purpose of this study was to obtain new information for a better understanding of the Badran deposit genesis.

In this paper, based on detailed fieldwork in underground mine workings, we present a brief summary of data on the geology of the deposit and new results of studying the material composition of disseminated and vein mineralization, geochemical, stable S and O isotopes, and the fluid inclusion microthermometry data for understanding ore-forming events and reinterpretation of the source of gold and the hydrothermal fluid-flow processes that formed orogenic Au Badran deposit in the context of the evolution of the surrounding accretion-collision structures of the Verkhoyansk-Kolyma orogen.

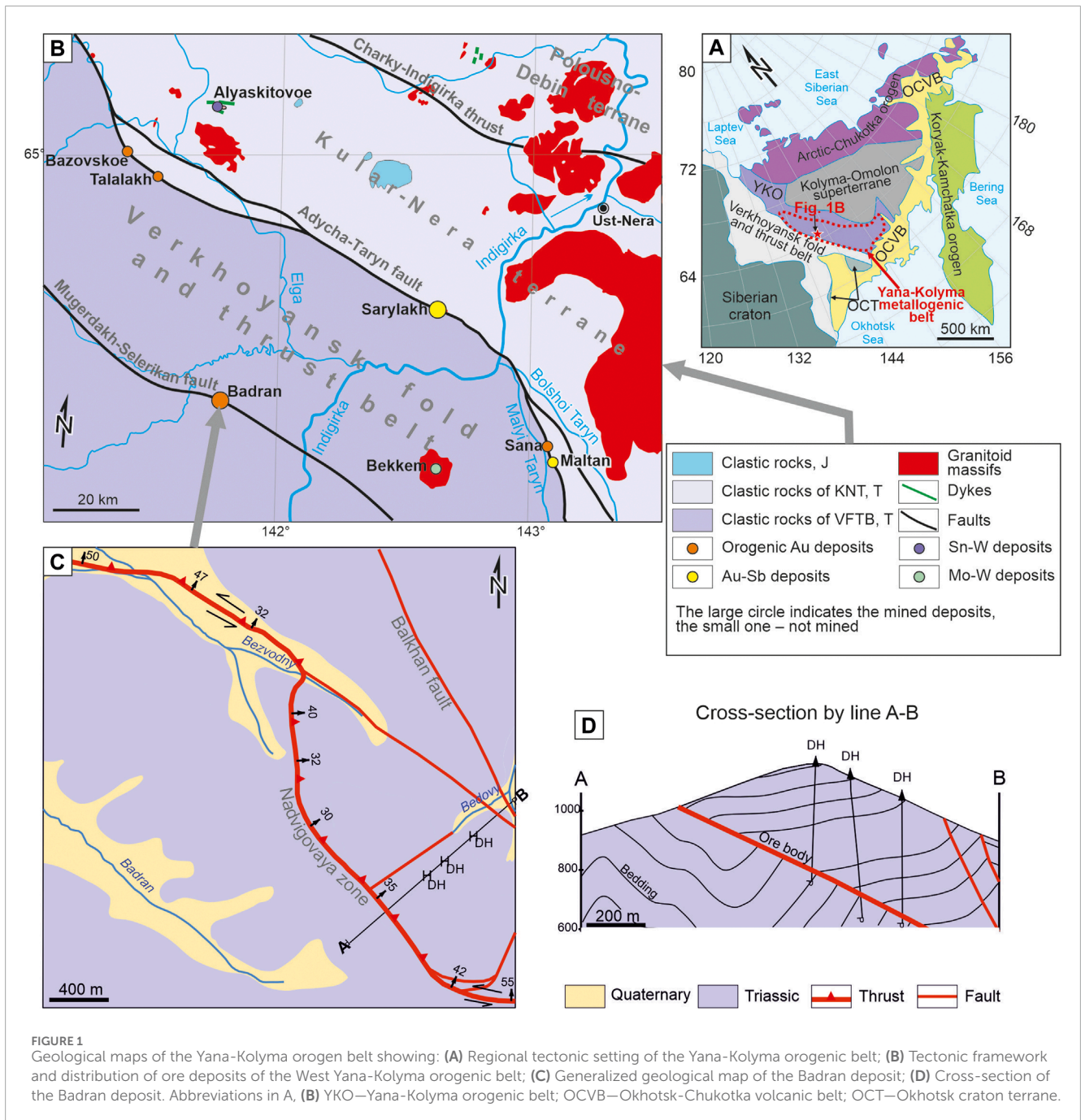
2 Regional tectonic and metallogenic setting

The Badran Au deposit is located in the rear of the Verkhoyansk fold-and-thrust belt to the southeast of the Yana-Kolyma orogen (Figure 1A). The Verkhoyansk fold-and-thrust belt lies on the Archean-Proterozoic basement and is composed of the Mesoproterozoic–Devonian carbonate-clastic and carbonate rocks and the Carboniferous–Middle Jurassic clastic rocks of the passive continental margin of the Siberian craton. The Verkhoyansk fold-and-thrust belt is separated from the Yana-Kolyma orogen by the regional Adycha-Taryn fault with an NW orientation and a length of about 2,000 km. The Yana-Kolyma orogen includes the Late Jurassic terranes of various origins (Khanchuk, 2006) (Figure 1A). Deformation processes and magmatism in the orogen in the Late Jurassic–Valanginian is related to the closure of the small Oymyakon paleocean and the subsequent collision of the Kolyma-Omolon superterrane and the eastern margin of the Siberian craton (Parfenov and Kuzmin, 2001; Goryachev and Pirajno, 2014).

The Yana-Kolyma metallogenic belt (YKMB) is identified mainly in the structures of the Kular-Nera and Polousno-Debin terranes of the Yana-Kolyma orogen and the rear zone of the Verkhoyansk fold-and-thrust belt. The belt stretches in the NW direction for more than 1,000 km with a width of up to 200 km to the SW from the Main Kolyma batholith belt (154–144 Ma, zircon, U-Pb SHRIMP-RG (Akinin et al., 2009), SHRIMP-II (Gertseva et al., 2021)), and Uyandina-Yasachnaya volcanic arc (152–153 Ma, zircon, U-Pb SHRIMP (Toro et al., 2016)). Metallogenic specialization of the Badran deposit area is determined by gold (Badran, Drazhnoye, Malo-Tarynskoe, Basovskoe, Talalakh, etc.) and Au-Sb (Sarylakh, Maltan, Kim, Vzbroz-2, etc.) deposits and less than W-Sn (Alyaskitovoe), Mo-W (Bekkem) deposits. Quite often, the orogenic gold deposits of the region show the overlap of late Au-Sb and Ag-Sb mineralization associated with the development of the Cretaceous Paleo-Pacific active continental margin.

The main structures of the Badran deposit area are determined by systems of extended NW thrusts and linear folds. They are separated by vast fields with gentle and near horizontal occurrence of rocks. Transverse NE and NS faults (oblique ramps), mainly of strike-slip and normal-strike-slip fault kinematics, dividing the thrusts into separate segments, are also identified. Thrusts are the main ore-controlling structures. The longest (about 20 km) is the Badran-Egelyakh thrust of the Mugurdakh-Selerikan fault system. The faults are expressed by thick (up to the first tens of meters) zones of brecciation of clastic rocks and are accompanied by folds with horizontal and inclined (up to vertical) hinges. Differently directed movements are identified along the faults—early thrust and late sinistral- and dextral-strike-slip faults, studied in detail at the gold deposits of the Kular-Nera terrane (Fridovsky et al., 2014; Fridovsky et al., 2015; Fridovsky et al., 2017; Fridovsky, 2018).

Magmatic formations do not occur at the Badran deposit. To the northeast of the deposit, there are the Late Jurassic



intrusive rocks and volcanic rocks of the intermediate and felsic composition of the Tas-Kystabyt belt (151–148 Ma, zircon, U-Pb SHRIMP-II (Prokopiev et al., 2018; Gertseva et al., 2021) and the Late Cretaceous granitoids of the Yus-Kuel complex (92–88 Ma, zircon, U-Pb SHRIMP-II (Protopopov et al., 2019)). Orogenic Au mineralization often involves the Late Jurassic-Early Cretaceous granitoids of small massifs and dikes from the mafic to the felsic composition of the complex of small intrusions (151–143 Ma, zircon, U-Pb SHRIMP II (Fridovsky et al., 2020a; Fridovsky et al., 2020b; Fridovsky et al., 2022)). These rocks were formed from a mixed source with the involvement of the mantle (OIB- and E-MORB type),

lower-crust and subduction components with the Mesoproterozoic-Paleoproterozoic Sm-Nd model estimates of the age of their magmatic sources (Fridovsky et al., 2020a; Fridovsky et al., 2020b; Fridovsky et al., 2022).

There is usually no spatial connection between gold deposits and magmatism and metamorphism. The deposits were formed after basic and granitoid magmatism (about 150 million years), superimposed on regional metamorphic changes in clastic rocks of the greenschist facies. The metallogenic time of formation of the gold mineralization is synchronous to the late collisional event of the end of the Tithonian-Valanginian during crustal thickening before the orogen collapse. Such conditions are characteristic of orogenic gold

mineralization events in accretion-collision orogens (Goldfarb and Groves, 2015; Yang et al., 2021).

Dating of micas ($^{40}\text{Ar}/^{39}\text{Ar}$) and native gold (Re-Os) from ore veins of orogenic gold deposits in the western part of the YKMB demonstrate a wide range of tectonothermal events that occurred from 148 to 126 million years (Fridovsky et al., 2015; Fridovsky et al., 2021; Fridovsky et al., 2022; Prokopiev et al., 2018). These events correlate with various tectonic processes on the eastern periphery of the Siberian craton in the Late Jurassic-Early Cretaceous. Isotopic Re-Os estimates of the age of gold (148 and 137 million years) (Fridovsky et al., 2021) coincide with the time of formation of dikes (151–145 million years) and cooling of granitoids of the small intrusions complex (138–137 million years) (Fridovsky et al., 2022) and reflect two stages of the formation of orogenic gold mineralization of the western part of the YKMB in connection with accretion-collision events on the eastern margin of the Siberian craton. According to the new $^{40}\text{Ar}/^{39}\text{Ar}$ geochronological data, for sericite from alterations, as well as feldspars and plagioclase from dikes of gold ore and gold-antimony deposits of this belt, the interval of 132–123 million years reflects the young tectonothermal processes of the final stage of the formation of gold mineralization (Fridovsky et al., 2022). These data are fit to the available age estimates for sericites from veins [126–127 Ma, $^{40}\text{Ar}/^{39}\text{Ar}$ (Fridovsky and Zaitsev, 2018; Prokopiev et al., 2018)] and granitoids [120–128 Ma, Rb-Sr and K-Ar (Zaitsev et al., 2018)] of various ore objects of the western part of the Yana-Kolyma metallogenic belt. The Hauterivian-Aptian event was probably a reflection of superimposed tectonic thermal processes occurring in the rear of the Uda-Murgal volcanic-plutonic belt. Thus, the features of the structure and metallogeny of the area of the Badran and YKMB deposits are associated with a complex interaction in the Late Jurassic to Early Cretaceous of subsynchronous geodynamic events on the eastern margin of the Siberian craton (subduction of the Oymyakon Ocean plate, accretion and collision of the Kolyma-Omolon superterrane) and Northern Asia (subduction of the Paleo-Pacific plate accretion (Parfenov and Kuzmin, 2001)).

3 Deposit geology

The Badran deposit is confined to the Nadvigovaya zone, the most ore-bearing section of the Badran-Egelyakh fault. The thickness of the thrust zone is up to 30 m. The displacement amplitude is estimated from 600 to 1,300 m (Anisimova et al., 1998; Neustroev, 2003). Several segments of the zone of different occurrence have been identified (Figure 1C). The north-western segment (survey profiles 0–250) occurs in the valley of the Bezvodny Creek. The Nadvigovaya zone here dips to C (5–20) at an angle of 30–50. The central segment (survey profiles 250–420) is the most ore-bearing, the zone dips gently to the NE (40–65), and the angle of dip is 24–30. The occurrence of the southeastern segment (east of the 420-survey profile) is similar to the NW segment—dipping to N (355–20), and the angle of dip is 30–50. Analysis of fractured structures and reconstruction of local tectonic stress fields showed changes in their orientation and kinematics in various segments of the Nadvigovaya zone (Fridovsky, 1999). There are thrust displacements for the central segment: NE-SW orientation

of the compression axis and a near-vertical or steeply inclined (65–70) plunge of the extensional axis to the NE or SW. The NW and SE segments are characterized by strike-slip reverse fault movements similar to the central segment by the position of the compression axis, a gently inclined (20–28) plunge of the extensional axis.

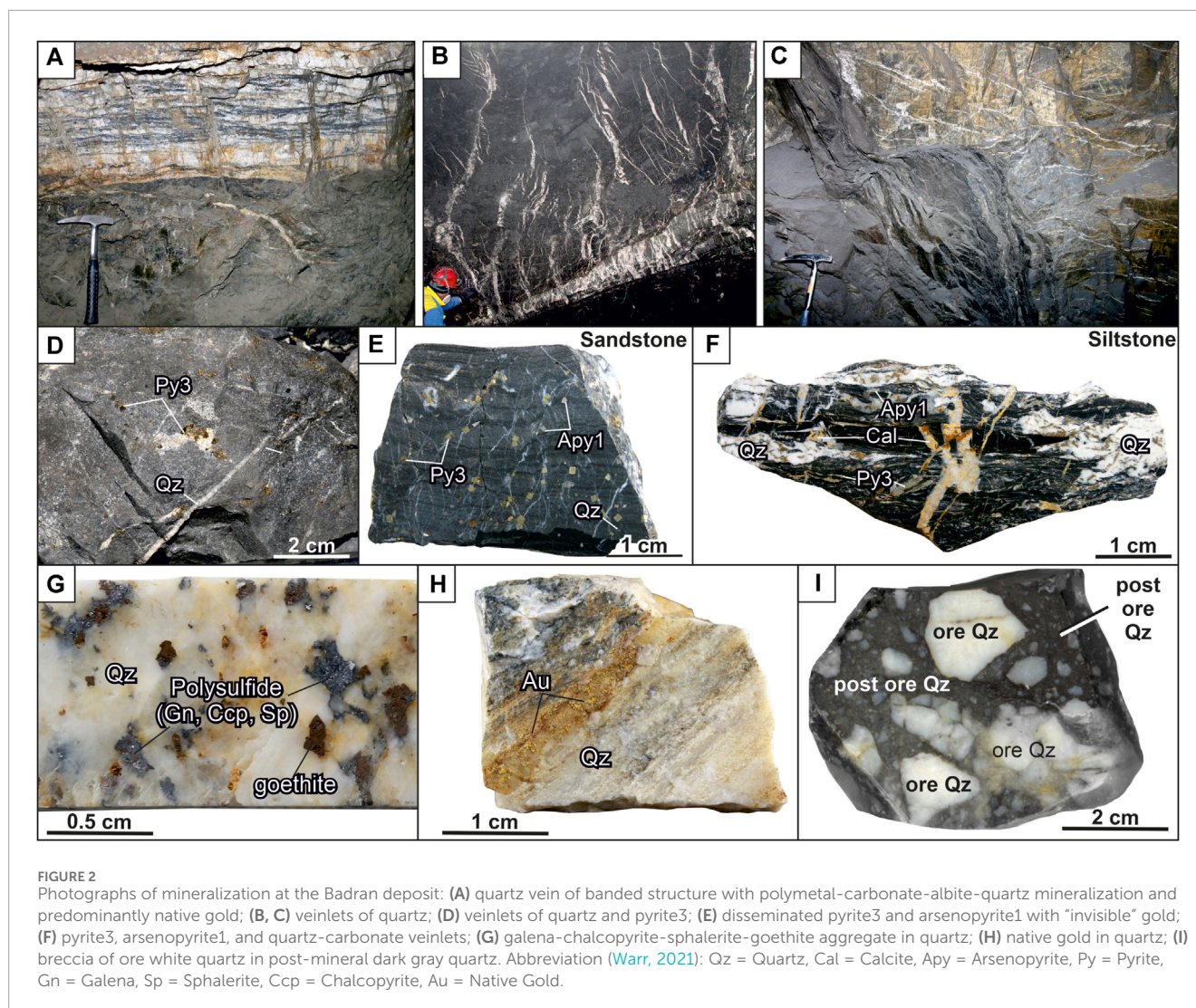
The Nadvigovaya zone is composed of breccias of host rocks with vein-veinlet and disseminated gold-bearing pyrite-arsenopyrite mineralization (Figure 2). The folded structures of the deposit area are represented by the Mugurdakh syncline, Talnakh, and Selerikan anticlines of the NW strike, extending up to 120–200 km (Neustroev, 2003). The southwestern wing of the Talnakh anticline is thrust over the Badran-Egelyakh fault onto the structures of the Mugurdakh syncline. The latter has an asymmetric structure, the southwest wing is characterized by gentle (20–25) rock dips, and the northeast—moderately steep (30–45) ones. In the zone of the Badran-Egelyakh thrust, the near-fault compressed folds of the NW and NE strikes are developed (Fridovsky, 2018). Here, the angle of dip of the rocks on the wings of the folds increases to 80°, and overturned occurrences are manifested.

The host rocks are the Norian clastic deposits (sandstones, silty sandstones, and siltstones) of the Upper Triassic with a total thickness of more than 3,800 m. Vein-veinlet mineralization is most intensively developed in sandstone beds, and their contacts with siltstones determine the position and morphology of sheet ore bodies. Ore-bearing rocks are metamorphosed to the level of carbonate-sericite-chlorite and chlorite-carbonate subfacies of the greenschist facies. Proximal alterations of sericite-chlorite-carbonate-quartz composition with highly gold-bearing disseminated pyrite and arsenopyrite are widely manifested in clastic rocks.

Three main morphological types of ore bodies are identified at the deposit: vein, vein-veinlet, and vein-disseminated (Figure 2). Quartz veins of a tabular shape are the leading type of ore bodies (Figure 2A). Their thickness is up to several meters, strike extent is tens of meters, and dip extent—hundreds of meters. Veins usually lie in the axial part of the Nadvigovaya zone, less often in its footwall or hanging contacts. In the upswells of the Nadvigovaya zone, branching and several parallel veins are observed. In the outcrops of veins and their flanks, the number of quartz veinlets increases (vein-veinlet type), and massive and coarse-banded structures of veins are replaced by veinlet and breccia ores (Figure 2B, C). The veinlet-disseminated type is represented by breccias and alterations with veinlet silification (from 5% to 40%) and impregnations of pyrite and arsenopyrite (Figures 2D–F). The content of “invisible” gold in pyrite and arsenopyrite is up to the first hundred grams per ton. In quartz veins and veinlets, gold is free, its content ranges from the firsts to hundreds of ppm and is associated with galena, sphalerite, and chalcopyrite (Figures 2G, H).

4 Mineralogy and paragenetic sequence

The ores of the Badran deposit are characterized by an exceptionally diverse mineral composition (Anisimova et al., 2008). About 50 hypogene and hypergene minerals are described here. Eight different stages of mineral formation were macroscopically and microscopic studies described in the Badran gold deposit, as



illustrated in Figure 3. There are four ore and four post-ore stages of mineral formation.

Metasomatic pyrite-arsenopyrite association in proximal sericite-chlorite-carbonate-quartz alterations is widespread. The typomorphic minerals of the association are gold-bearing pyrite3 (Au up to 120 ppm) and arsenopyrite1 (Au up to 205 ppm), which form dispersed dissemination of metacrystals in ore zones and in host rocks (Figures 2D–F; Figures 4C, D). This gold1 is in an “invisible” form (Fridovsky et al., 2022). Arsenopyrite1 is found everywhere, but less often than pyrite3. Arsenopyrite1 forms dispersed dissemination of idiomorphic prismatic crystals in quartz-bearing siltstones (Figures 2E, F). Radial growths of small crystals of arsenopyrite are characteristic. Often crystals are cataclastic (Figure 4D). Quartz1, carbonate, and sericite are associated with pyrite3 and arsenopyrite1 (Figures 2D–F). Pyrite1 and Pyrite2 are also found in altered rocks. Pyrite1 is represented by dust-like and fine-grained spherical (framboidal) particles and nodular aggregates ranging in size from 10 to 100 microns (Figures 4A, B). The location of Py1 follows the primary sedimentary texture of rocks. Metamorphic pyrite2 represented by crystals with subhedral and euhedral shapes, ranging in size from 2 to 3 microns to 2–4 mm,

which form dissemination intergrowths, nests, and thin veinlets (Figures 4A, B) (Fridovsky et al., 2022).

Arsenopyrite-pyrite-carbonate-quartz vein association is the most common in ore bodies. Native gold of this association is usually represented by finely dispersed idiomorphic crystals and lumpy varieties of gold (Figure 2H). Quartz2 of the main producing association has an inequigranular and hypidiomorphic structure. Color is milky-white, grayish-white, and, rarely, white. In the selvages of veins and veinlets, as well as near the xenoliths of the host rocks, this quartz often has a crustified texture, and in the central part, a massive and knotted texture. The structure of the aggregate is hypidiomorphic-granular. Vein pyrite4 has, basically, an irregular shape (Figures 4E, F). It is characterized by a high gold content, sometimes reaching hundreds of ppm, but on average tens of ppm, the silver content of pyrite is next lower order. A typomorphic feature of pyrite4 is its increased arsenic content. Arsenopyrite2 is developed in quartz veins and is often found with Py4 (Figures 4E, F). Apy2 is surrounded by late minerals—chalcopyrite and fahlore often associate native gold with arsenopyrite (Figure 4G). The composition of arsenopyrite2 is characterized by high sulfur content and low arsenic content. The

Stage	Hypogene (hydrothermal)					Supergene		
	Ore				Post-ore			
Association	Metasomatic Py-Apy	Apy-Py-carbonate-quartz	Polymetallic-carbonate-albite-quartz	Sulfostibnite-sericite-quartz	Silver-quartz	Cinnabar-stibnite-carbonate-quartz	Sulfur-sulfate	Oxide
Minerals								
Quartz	———— ¹	————	-----	-----		
Carbonate	————	————	-----	-----	-----		
Albite		-----					
Sericite	-----	————	-----			
Native gold		————	————	————	-----	
Pyrite	————	————	-----	-----		
Arsenopyrite	————	————	-----	-----		
Galena			————	-----				
Sphalerite			————	-----				
Chalcopyrite			————	-----				
Tetrahedrite				————				
Sulfosalts Pb				————				
Freibergite					————			
Acanthite					————			
Sulfosalts Ag							
Stibnite						————		
Cinnabar						————		
Gypsum							————	
Jarosite							————	
Anglesite							-----	
Cerussite							
Goethite								————
Servantite								————
Tripugit								————
Polyanite							
Malachite							
Azurite							
Skorodite							
Kaolinite								-----
Utenbogaardtit						

¹ The width of the lines represents relative abundance of minerals

FIGURE 3
The paragenetic sequence of ore minerals and some gangue minerals in the Badran gold deposit.

mineral is characterized by high gold content, reaching hundreds of ppm. Native gold² is common in minerals of the early arsenopyrite-pyrite-carbonate-quartz association of vein filling (Figures 5A, B). A significant part of it is also in a finely dispersed form.

Polymetal-carbonate-albite-quartz mineral association is mainly distributed on the flanks of the upper horizons of the Nadvigovaya

zone. At deep horizons, it is found in the central part of ore columns. Quartz³ of a sugar-like habit composes separate veins and veinlets. The proportion of this quartz in the vein filling ranges from 15% to 30%. Typomorphic minerals are chalcopyrite, galena, sphalerite, gold, dolomite, and albite (Figure 2G; Figure 4H). Galena is a minor mineral. The frequency of its occurrence increases with

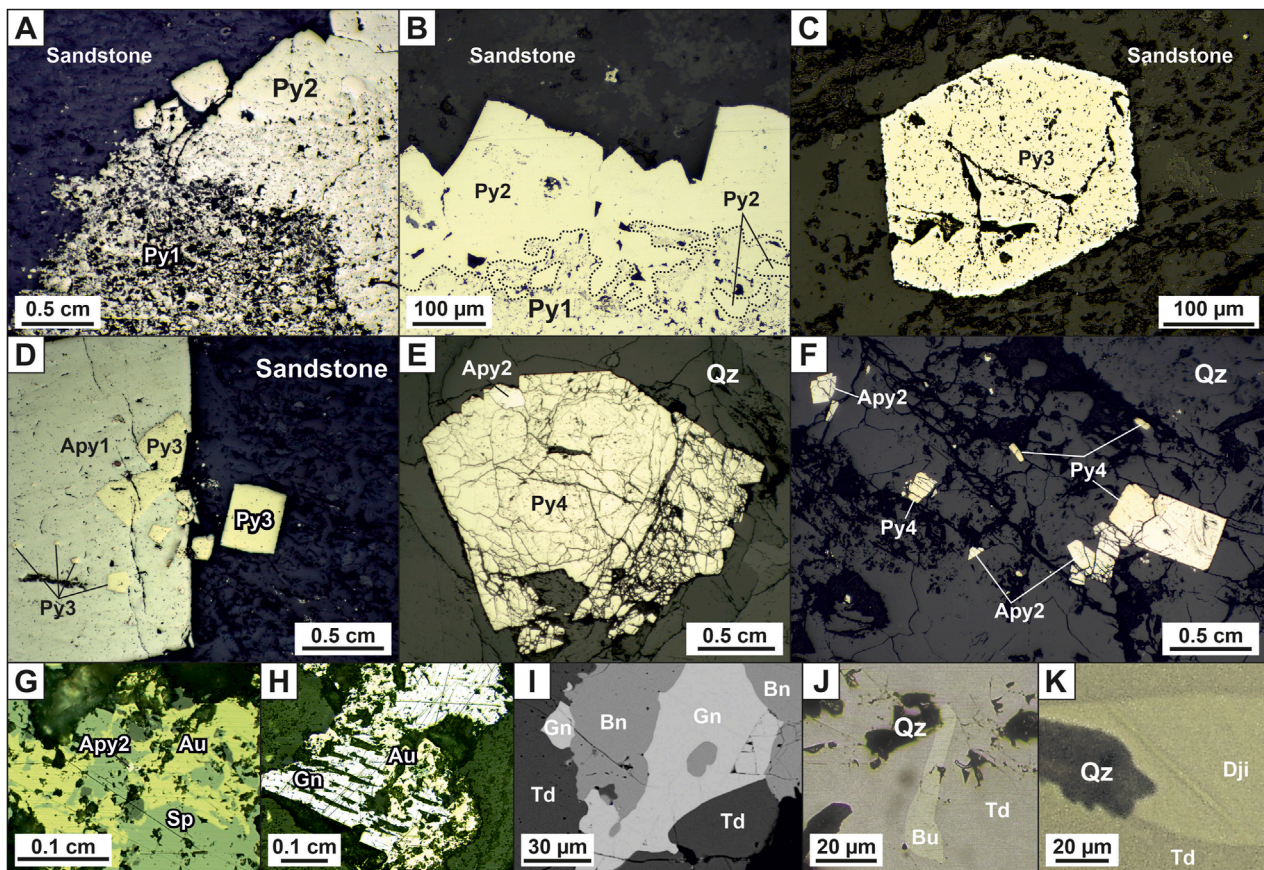
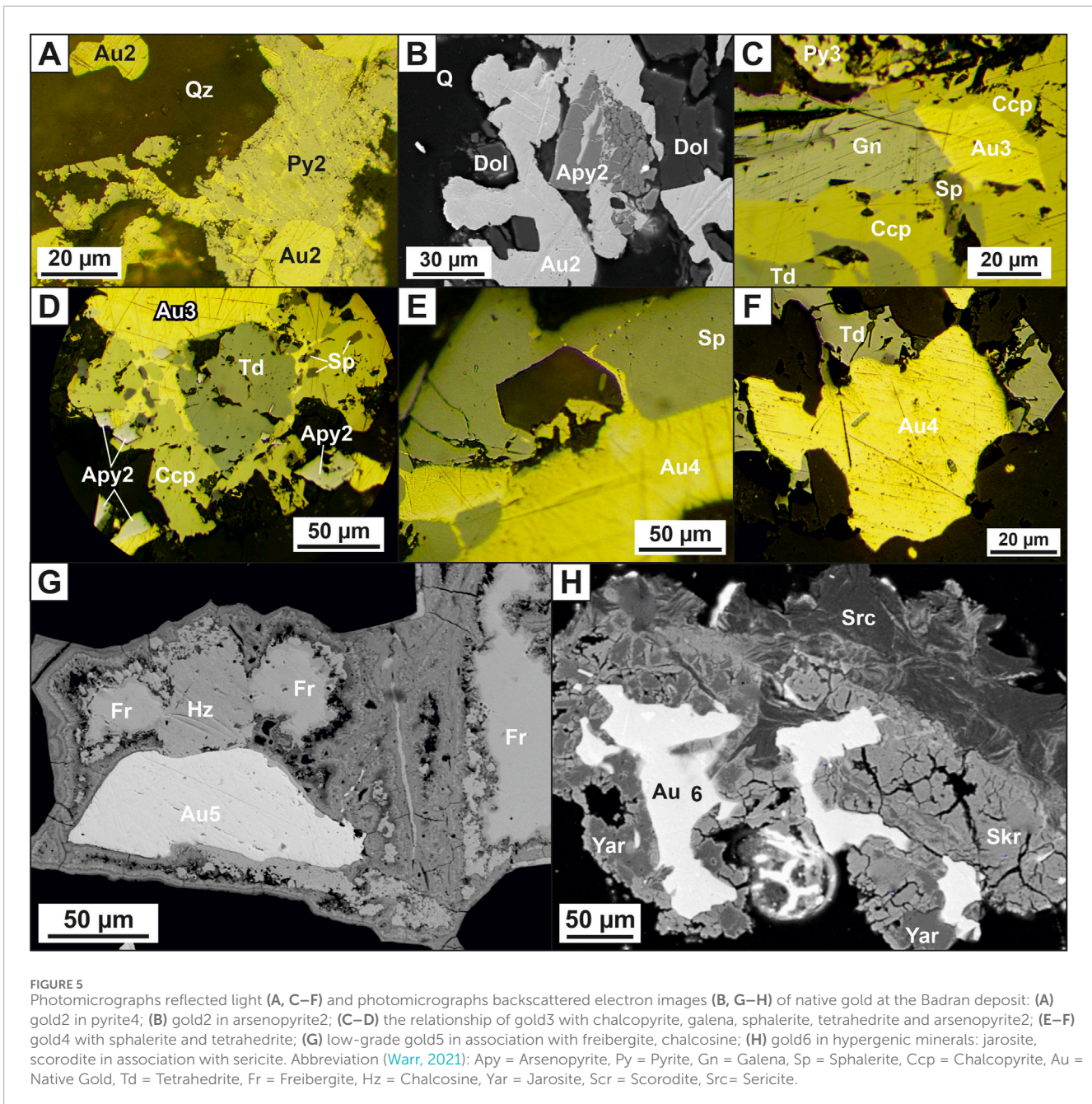


FIGURE 4
Photomicrographs reflected light (A–H) and photomicrographs backscattered electron images (I–K) disseminated and vein ores at the Badran deposit: (A, B) pyrite1 and pyrite2 intergrowths in sandstone; (C) pentagonal dodecahedral crystal of pyrite3 from proximal alteration; (D) pyrite3 intergrowths in arsenopyrite1, and separate pyrite3 crystals in sandstone; (E) crushed pyrite4 crystal with arsenopyrite2 in quartz; intergrowths and separate crystals of arsenopyrite2 and pyrite4 in quartz; (G) native gold in association with sphalerite and arsenopyrite2; (H) gold with galena; (I) overgrowth of galena with bournonite and tetrahedrite; (J) inclusion of bournonite in tetrahedrite; (K) diamond-shaped jamesonite in tetrahedrite. Abbreviation (Warr, 2021): Qz = Quartz, Cal = Calcite, Apy = Arsenopyrite, Py = Pyrite, Gn = Galena, Sp = Sphalerite, Ccp = Chalcopyrite, Au = Native Gold, Bu = Bournonite, Td = Tetrahedrite, Bu = Boulangerite, Dji = Jamesonite.

depth. It is associated with sphalerite, chalcopyrite, bournonite, fahlore, and native gold (Figures 4G, H; Figure 5C). Galena in the deposit contains bismuth and silver in the form of an impurity, the concentration of which disappears with depth. Sphalerite occurs in quartz in the form of irregularly shaped particles and scattered single crystals of yellowish-brown color, which is explained by low ferruginosity. It is associated with galena, chalcopyrite, bournonite, fahlore, and native gold (Figures 4G, 5C–E). Chalcopyrite is observed in quartz in the form of small irregularly shaped particles and emulsion dissemination of chalcopyrite in sphalerite and fahlore. The frequency of occurrence of chalcopyrite in association with native gold increases with depth (Figures 5C, D). Gold3 (fineness from 800‰ to 899‰) is associated with the main minerals, chalcopyrite and galena. In this case, chalcopyrite always acts as the host mineral, and galena forms close growths with gold (Figures 5C, D).

Sulfostibnite-sericite is a quartz mineral association with an admixture of rare sulfostibnites, characterized by an increase in the potential of antimony and sulfur. It occurs in the central

most ore-bearing interval of the Nadvigovaya zone. Quartz4 is an ore-free milky white that mainly associates with carbonate and chlorite. On the contacts of the veins, such quartz usually has a comb structure. Tetrahedrite, gold, and sericite are typomorphic minerals. Tetrahedrite forms xenomorphic inclusions, veinlets, and granular aggregates in quartz in associations with native gold, bournonite, galena, and chalcopyrite (Figures 4I–K; Figure 5F). The silver content in tetrahedrite varies widely from 0% to 9.72%. Tetrahedrite, as a rule, is oxidized with the formation of thin rims, falsers of malachite, azurite, chalcosine, and covellite. The native gold (Au4) of this association is the most high-grade (900‰–998‰), it is predominantly interstitial, lenticular, wedge-shaped, ribbon-shaped, and lump-shaped (Figures 5E, F). The mineral associations described above are the most economically important. They formed the ore columns of the Badran deposit. The formation of pyrite five to six completes orogenic ore formation at the deposit. Pyrite five to six forms a rare euhedral and subhedral dissemination and is related to polymetallic-carbonate-albite-quartz and sulfostibnite-sericite-quartz mineral associations, respectively.



Silver-quartz and cinnabar-stibnite-carbonate-quartz mineral associations are widespread locally. Freibergite, acanthite, argentotetrahedrite, and low-grade mercury gold (400‰–700‰) are the typomorphic minerals of the silver-quartz association. The dark gray–black quartz₅₋₆ of this association cements fragments of early white quartz (Figure 2I). The fahlore of the Badran deposit have an abnormally high silver content (>30%). It does not form large accumulations and occurs in growth with argentite, electrum, native gold, freibergite, and tetrahedrite. Sporadic veinlets of a typomorphic mineral of another association, stibnite with idiomorphic water-transparent quartz and dolomite nests, occupy a crosscutting position in relation to early paragenesis. Signs of

cinnabar are found on the near-surface horizons of the deposit. Freibergite (Ag–10%–29%) occurs at the upper horizons, it forms close growths with tetrahedrite. Acanthite and low-grade native gold are often associated with it. Acanthite forms granular aggregates and sometimes myrmekitic growths with freibergite. In association with acanthite, bournonite and low-grade native gold (Au₅) are also found in the ore (Figure 5G). Acanthite contains impurities of Fe, Sb, and Cu. It is likely that such a set of elements can be explained by the close association of acanthite with fahlore. Native gold has not been identified in this association. Pyrite 7–8 forms cogenetic growths with the minerals of silver-quartz and cinnabar-stibnite-carbonate-quartz associations.

TABLE 1 Statistical values of EPMA analyses of pyrite3 and arsenopyrite1 from proximal alterations of the Badran gold deposit (wt%).

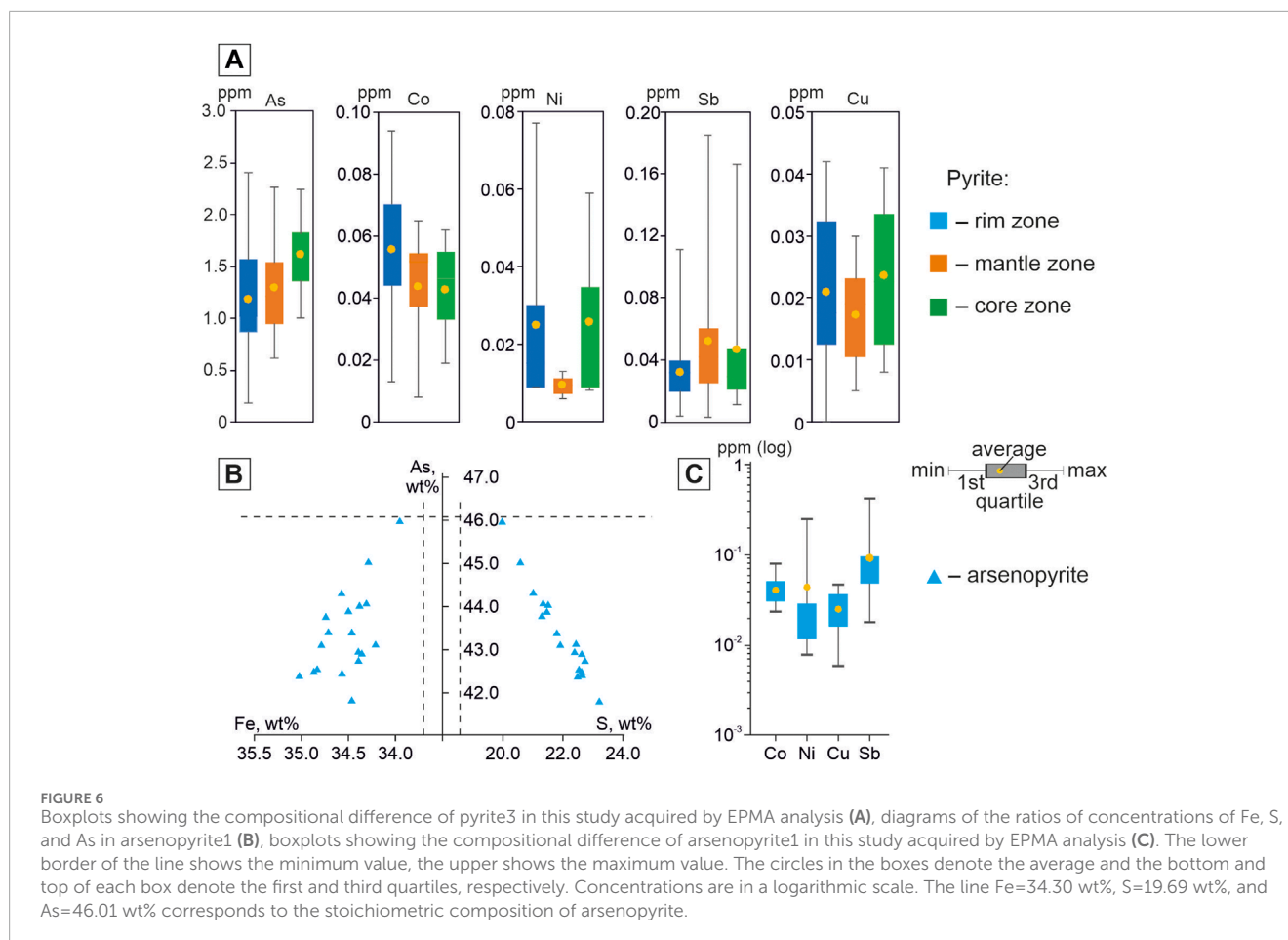
Place and number of measurements	Index	Fe	S	As	Co	Ni	Cu	Sb	Pb
Zonal grains of metasomatic pyrite3									
Rim zone <i>n</i> = 28 ^a	Minimum (<i>C</i> _{min})	45.38	51.82	0.18	0.01	0.01	0.01	0.01	0.01
	Maximum (<i>C</i> _{max})	46.49	54.17	2.41	0.09	0.28	0.04	0.11	0.09
	Average (<i>C</i> _{av})	45.93	52.76	1.19	0.06	0.05	0.02	0.03	0.04
	Median (<i>Me</i>)	45.93	52.89	1.02	0.06	0.02	0.02	0.03	0.03
	Standard deviation (σ)	0.29	0.53	0.57	0.02	0.08	0.02	0.02	0.03
	Coefficient of variation (<i>V</i> _{σ})	1	1	56	39	533	91	72	101
Mantle zone; <i>n</i> = 15	Minimum (<i>C</i> _{min})	45.50	51.76	0.62	0.01	0.01	0.01	0.01	0.01
	Maximum (<i>C</i> _{max})	46.31	53.25	2.27	0.07	0.02	0.03	0.19	0.05
	Average (<i>C</i> _{av})	45.98	52.60	1.30	0.04	0.01	0.02	0.06	0.03
	Median (<i>Me</i>)	45.96	52.55	1.22	0.05	0.01	0.02	0.05	0.03
	Standard deviation (σ)	0.23	0.44	0.49	0.02	0.00	0.01	0.05	0.02
	Coefficient of variation (<i>V</i> _{σ})	1	1	41	33	46	47	100	53
Core zone; <i>n</i> = 12	Minimum (<i>C</i> _{min})	45.39	51.93	0.98	0.02	0.01	0.01	0.01	0.01
	Maximum (<i>C</i> _{max})	46.39	53.01	2.24	0.06	0.06	0.04	0.17	0.11
	Average (<i>C</i> _{av})	45.83	52.44	1.60	0.04	0.02	0.02	0.05	0.05
	Median (<i>Me</i>)	45.77	52.38	1.61	0.05	0.02	0.01	0.03	0.05
	Standard deviation (σ)	0.30	0.34	0.38	0.01	0.02	0.01	0.05	0.04
	Coefficient of variation (<i>V</i> _{σ})	1	1	24	31	95	103	145	112
Metasomatic arsenopyrite1									
<i>n</i> = 20	Minimum (<i>C</i> _{min})	33.95	19.96	41.81	0.02	0.01	0.01	0.02	bdl ^b
	Maximum (<i>C</i> _{max})	35.03	23.21	45.98	0.08	0.25	0.05	0.43	bdl
	Average (<i>C</i> _{av})	34.52	21.90	43.39	0.04	0.04	0.03	0.10	-
	Median (<i>Me</i>)	34.47	21.90	43.13	0.04	0.02	0.03	0.06	-
	Standard deviation (σ)	0.26	0.83	1.02	0.01	0.07	0.01	0.10	-
	Coefficient of variation (<i>V</i> _{σ})	1	4	2	35	431	54	173	-

^a*n* = number of analysis.

^bbdl = below detection limit.

In the process of hypergenesis, there was a change in ores and the formation of two mineral associations of *sulfur-sulfate and oxide compositions*. The typomorphic minerals of the first association are gypsum, jarosite, anglesite, covellite, and chalcocite; those of the second are goethite, hydrogoethite, malachite, azurite, cervantite, triphuyite, polianite, and uytensbogaardtite. They develop when pyrite, arsenopyrite, chalcopyrite, iron-magnesian dolomite,

and mica minerals are replaced. At deep horizons, gypsum and iron hydroxides and oxides are noted in hypergenic minerals. Gold and silver sulfides in the ores of the Badran deposit were found at the horizon of 940–960 m of ore column I in association with high-silver fahlore, acanthite, pyrrargyrite, bournonite, galena, various mercurous native gold, anglesite and close growth with hypergene minerals. Considering chemical



composition, the analyzed compounds cover the entire interval between AgAuS and Ag_3AuS_2 , but differences predominate, tending to the silver analog uytenbogaardtite. Au and Ag sulfides of the Badran deposit, in our opinion, were formed due to native gold and hypogene changes in high-silver fahlores, as evidenced by the ubiquitous joint presence of uytenbogaardtite with oxides of Sb and Fe with the admixture of Ag, Cu, and As. Native gold of the sixth generation (Au_6) occurs with minerals of the hypogene stage, mainly with iron hydroxides, scorodite, and jarosite, and sometimes has a spongy habit (Figure 5H). This gold often forms thread-like veinlets in iron hydroxides with arsenopyrite relics.

5 Samples and analytical methods

5.1 Sample preparation

More than 200 ore samples were selected from the rich areas of the ore bodies of the Badran deposit to study the mineral composition and stable isotope analysis and fluid inclusion. All monofractions of minerals were hand-picked with a binocular microscope. The samples were crushed to 16–60 mesh size to ensure purity of >98%. Sixteen ore samples were subjected to S isotope analysis from a micro-weighted portion, and twenty by the *in situ*

method. Isotopic analysis of O quartz was performed in twelve ore samples. The study of the thermometry of fluid inclusions in quartz was performed in doubly polished sections (0.3–0.5 mm thick). Fluid inclusions were studied in twenty-two ore samples, selected at various depth levels from underground mine workings of the Badran deposit. Only in eight polished sections were inclusions with sufficient dimensions found.

5.2 Scanning electron microscope and electron probe microanalysis

The analyses of minerals were performed at the Diamond and Precious Metal Geology Institute, Siberian Branch, Russian Academy of Sciences (RAS), Yakutsk, Russia following the procedure of Kudrin et al. (2021). The qualitative chemical and mineral compositions of the samples were studied with the use of a JEOL JSM-6480LV scanning electron microscope (SEM) equipped with an Energy 350 Oxford energy dispersive spectrometer (acceleration voltage was 20 kV, current through the sample was 1 nA, beam diameter was 1 μm). The major element compositions of minerals were determined by standard X-ray spectral analysis on a Camebax-Micro electron probe microanalyzer (EPMA). The analytical conditions were as follows: accelerating voltage of 20 kV;

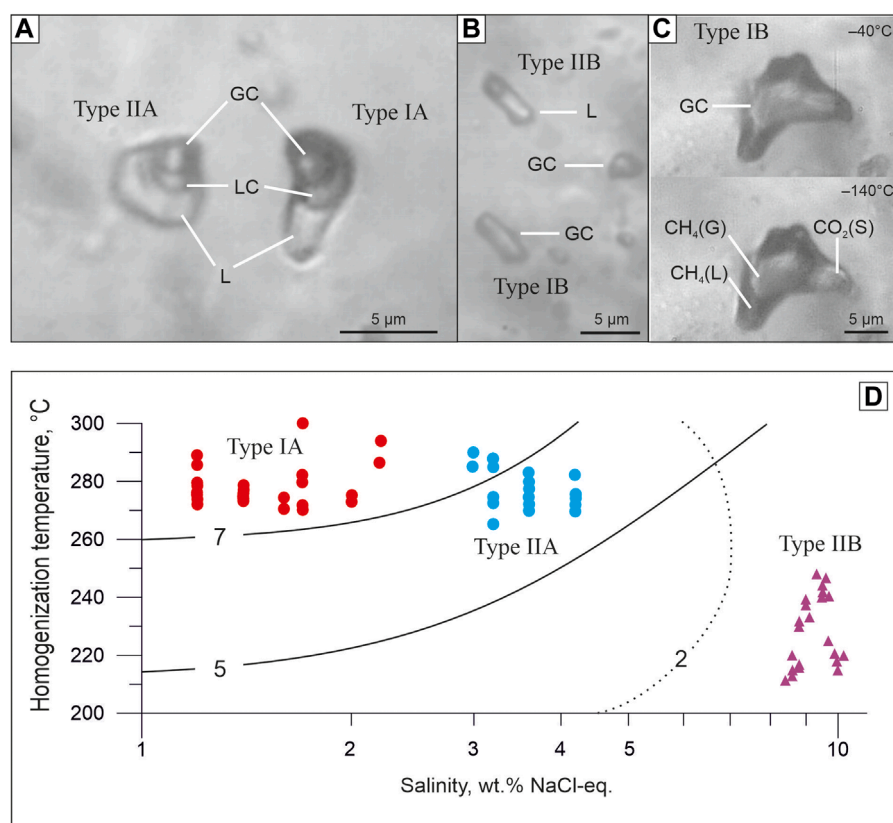


FIGURE 7

Micrographs of fluid inclusions in quartz from the Badran gold deposit. (A) The central zone of quartz crystals (type-IA + type-IIA); (B, C) the outer zone of quartz crystals (type-IB + type-IIB). Abbreviation: L—liquid H₂O. LC—liquid CO₂+CH₄. GC—gaseous CO₂+CH₄. CH₄(L)—liquid CH₄. CH₄(G)—gaseous CH₄. CO₂(S)—solid CO₂. (D)—Salinity-temperature diagram showing the data for type IA, IIA, and IIB fluid inclusions. Solid and dotted lines show CO₂ solubility in H₂O-NaCl solutions (mol%) under the pressure of 500 bars and 200 bars, respectively (Soloviev et al., 2019).

beam current of 25 nA; measurement time of 10 s; K series for Fe, Co, Ni, Cu, and S; M series for Au and Pb; L series for As and Sb; and wavelength-dispersive spectrometer (WDS) with LiF, PET, and TAP crystals. The standards used were: FeS₂ for Fe and S, FeAsS for As, Fe-Ni-Co alloy for Co, Ni, Au-Ag alloy of fineness for Au and Ag, CuSbS₂ for Sb, and PbS for Pb. The detection limit was 0.01%. In each grain, three measurements were made: rim, mantle, and core zone.

5.3 S–O isotope analysis

Isotopic analysis of δ³⁴S in sulfides (58 samples) and δ¹⁸O in quartz (12 samples) was performed in the Laboratory of Stable Isotopes of the Far Eastern Geological Institute, Far Eastern Branch of the Russian Academy of Sciences (RAS), Vladivostok, Russia.

5.3.1 Sulfur Isotope Analysis

The Femtosecond laser-ablation fluorination method described in detail by (Ignatiev et al., 2018; Velivetskaya et al., 2019) was applied for *in situ* measurements of δ³⁴S values in sulfide minerals. Briefly, an ultraviolet femtosecond laser ablation system (NWR Femtosecond UC with laser Pharos 2mJ-200-PP, supplied by Electro

Scientific Industries New Wave Research Division, Portland, OR, USA) was used to produce a laser crater of approximately 80 μm diameter and 40 μm depth in pyrite. Laser-generated aerosol sulfide particles were converted to SF₆ via reaction with BrF₅ at 350°C. The SF₆ was purified by means of a cryogenic trap system (Velivetskaya et al., 2019) and introduced into the ion source of a Thermo Scientific MAT 253 isotope ratio mass spectrometer using a gas injection interface developed and described by (Ignatiev et al., 2018). Sulfur isotope ratios were measured by monitoring the SF₅⁺ ion currents at mass-to-charge ratios of *m/z* 127 (³²SF₅⁺) and 129 (³⁴SF₅⁺). All sulfur isotope data are presented as conventional notation δ³⁴S and reported relative to Vienna Cañon Diablo Troilite (V-CDT). Three International Atomic Energy Agency standards IAEA S1, S2, and S3 (Ag₂S powder) were used to calibrate the SF₆ reference gas and in-house standard (pyrite). Analytical precision of ±0.2‰ (1σ) for δ³⁴S values was estimated from the long-term (approximately 1-year-long period) reproducibility of in-house standard (Velivetskaya et al., 2019). It should be noted that the method does not require the use of any correction factors for the effect of a laser-induced isotope fractionation due to the use of a femtosecond laser, which eliminates the effect of heating of crater walls and dramatically reduces the dependence of isotope fractionation on

TABLE 2 Results of the microthermometry of fluid inclusions in quartz from the Badran deposit.

Sample no.	Phase transition temperatures, °C					Calculated parameters		
	T _i ^a	T _{gh}	T _{mit} CO ₂	T _{hom} C	T _{hom}	H ₂ O:CO ₂ :CH ₄ mole.% ^b V,cm ³ /mole ^c	NaCl wt.%-eq ^d	P bar ^e
Type-IA and type-IIA in the central zones of quartz crystals								
B-43-19	–	9.2	–58.5	13.5 (g)	280–300 (g)	$\frac{85 : 12.5 : 2.5}{43}$	1.6	250–300
	–	8.4	–59.6	15.5 (c)	280–290 (l)	93 : 6 : 1	3.2	
B-25-19	–	9.3	–59.0	10.5 (g)	270–280 (g)	$\frac{83 : 14 : 3}{43}$	1.4	250–300
	–	8.2	–59.5	13.0 (c)	270–280 (l)	93 : 6 : 1	3.6	
B-32-19	–	9.3	–59.2	12.7 (g)	270–280(g)	$\frac{82 : 15 : 3}{42}$	1.4	250–300
	–	8.2	–59.6	15.5 (c)	265–275(l)	93 : 6 : 1	3.6	
Type-IB and type-IIB in the outer zones of quartz crystals								
B-25-19	–	–	–61.5	–124(g)	–40.5(g)	$\frac{0 : 30 : 70}{330}$	–	125
	–5.5	–	–	–	210–220(l)	100 : 0 : 0	8.6	
B-43-19	–6.2	–	–	–	240–250	100 : 0 : 0	9.5	–
B-23-19	–	–	–62.2	–110(g)	–47 (g)	$\frac{0 : 25 : 75}{330}$	–	125
	–6.6	–	–	–	215–225	100 : 0 : 0	10.0	
B-39-19	–5.8	–	–	–	230–240	100 : 0 : 0	9.0	–

^aTemperatures: T_i—ice melting (±0.2°C), T_{gh}—gas hydrate melting; (±0.3°C), T_{mit}CO₂—carbon dioxide melting; T_{hom}C—homogenization of methane-carbon dioxide fluid into the gas (g) or critical (c) phase, T_{hom}—final homogenization of the inclusion to the liquid (l) or gaseous (g) phase. At least 5 individual inclusions were analyzed in each group.

^bThierry et al., 1994

^cRoedder, 1984.

^dBodnar and Vityk, 1994; Darling, 1991.

^eRoedder, 1984; Bakker, 2003.

the matrix (Fu et al., 2017), observed in the nanosecond laser ablation.

The external reproducibility of δ¹⁸O values was better than 0.1‰ for standards and 0.2‰ for the samples.

5.3.2 Oxygen isotope analysis

A laser fluorination system modified from Sharp (1990) directly coupled to a Thermo Scientific MAT 253 isotope ratio mass spectrometer was used. Approximately 1 mg of the sample was heated by a CO₂ laser (MIR-30, New Wave Research, United States) in the presence of BrF₅. The O₂ gas liberated from the sample was purified by passing through a series of liquid nitrogen traps, a KBr trap at 100°C, and through an HP-MOLSIV 30 m × 0.32 mm × 25 μm column. The oxygen isotope ratio of the O₂ gas was measured by the MAT-253 mass spectrometer running in continuous flow mode relative to the O₂ reference gas that was calibrated against the international standard NBS-28 and the standard at the University of Wisconsin UWG-2 garnet (Valley et al., 1995). Isotope values are given in the standard delta notation per mil (‰) versus VSMOW.

5.4 Thermometry and compositions of fluid inclusions

Microthermometric analyses of the fluid inclusions were made using the UMTK-3 freezing-heating stage designed by VIMS Institute and modified by TsNIGRI Institute, Russian Geological Survey, to allow low-temperature experiments. Low-temperature measurements were conducted first; cooling was by liquid N₂ flow. The stage employs a chromel-alumel thermocouple and is capable of attaining temperatures ranging from below –180 to over +650°C. The stage was periodically calibrated using the boiling temperature of pure N₂ (–196°C), triple point for pure CO₂ (–56.6°C), temperatures of ice melting in standard NaCl solutions

TABLE 3 Sulfur isotope compositions of ore sulfides from the Badran deposit.

Mineral	Description of samples	$\delta^{34}\text{S}_{\text{CDT}}$ (‰)	n
Arsenopyrite2	Quartz from the vein	1.1; 1.8; 2.3 ^a	3
Pyrite4	Quartz from the vein	1.7/1.1; 1.0/0.7; 1.4	5
Arsenopyrite3	Alterations on siltstone and sandstone	-1.1/-0.6; -0.7/-0.8; -0.5/-0.2; -0.4/-0.3; -0.4/0.1; -0.3/-0.3; -0.3/-0.2; 0.0/-0.3; -0.3/-0.3; 1.4; 2.4; 2.4	21
Pyrite3		-0.7/1.4; -0.5/1.0; -0.2/-0.3; 0.1/1.8; 0.3/0.3; 0.4/1.6; 0.5/1.8; 0.6/1.9; 0.8/1.1; 1.0/1.2; 1.0/0.7; 1.1/1.0; 1.5/1.5; 0.2; 0.4; 1.0; 1.4; 1.5; 1.5; 1.5; 2.0; 2.1	35

^aThe values of the isotopic composition determined by the *in situ* from two measurements made in the center (numerator) and on the periphery (denominator) of the grains are shown in italics. The rest are determined by the bulk method.

(from -18 to -1°C), melting temperatures of AgNO₃ (210°C) and K₂CrO₇ (398°C).

For bulk fluid inclusion analysis (Kryazhev et al., 2006), pure mineral concentrates of 1 g of quartz were prepared by handpicking under a binocular microscope and crushed in an agate mortar to 0.25–0.5 mm. This was followed by cleaning in an aqueous (1:1) HNO₃ solution and then by water-flow electrolytic cleaning in an ultrasonic bath for 3 h. Following this procedure, the samples were dried and put into a quartz glass reactor under vacuum at 110°C and then filled with helium. The fluid inclusions were heated to 500°C for 15 min. The gases extracted were introduced into a gas chromatograph (Agilent 6890) for determination of H₂O, CO₂, and CH₄. Then, the heated samples were leached with deionized water in an ultrasonic bath for 15 min. The leachate solution was separated by centrifuging and then analyzed by ion chromatography (TSVET3006) for anions (Cl, F, and SO₄) and by ICP-MS (Elan-6100) for other elements.

5.5 Gold content in sulfides

The content of Au in powdered monomineral samples of pyrite (12 pcs.) and arsenopyrite (9 pcs.) was determined by atomic absorption spectrometry with electrothermal atomization on a LUMEX MGA-1000 spectrometer (Russia) (DPMGI SB RAS). The lower limit of gold detection is 0.02 ppm.

6 Results

6.1 Chemical composition of pyrite and arsenopyrite from proximal alteration rock

In the sericite-chlorite-carbonate-quartz proximal alterations, arsenopyrite1 is represented by short-prismatic and pseudopyramidal crystals, pyrites are characterized by cubic and pentagondodecahedral forms (Figures 3C, D). There are fractured arsenopyrite1 and pyrite3 with inclusions of late sulfides (galena, sphalerite, chalcopyrite, etc.). Crystal size from 1–1.5 to 2–3 mm. Pyrite3 and arsenopyrite1 are characterized by disseminated, euhedral, and/or semieuhedral textures. The content of disseminated sulfide mineralization in proximal alteration is up to 6%–8%. Usually, pyrite prevails at a distance from quartz veins/veinlets, and arsenopyrite prevails near them. These minerals hosted invisible gold in the Badran deposit.

Supplementary Tables S1, S2 contain information about compositions (wt%) and Table 1 contains statistical characteristics (minimum values; maximum values, median, standard deviation, and coefficient of variation) for pyrite and arsenopyrite in the proximal alteration rock of the Badran deposit analyzed by EPMA. Pyrite of non-stoichiometric composition prevails (Fe/(As+S)≠0.50; S/Fe≠2.00). The main impurity in pyrite3 is As (C_{As} = 0.18–2.41 wt%) (Figure 6A).

Typomorphic impurities in pyrite3 are Co, Ni, Cu, Sb, and Pb (Figure 6A). Micro impurities of other elements are present in quantities below the detection limit of EPMA analyzes. The total impurity content varies from 0.01 to 0.37 wt% and the entire spectrum of elements is recorded in single crystals. The concentrations of impurity elements vary within large limits (Supplementary Tables S1, S2; Table 1), the most stable contents are characteristic of Co (V_σ = 31%–39%) and As (V_σ = 34%–56%). The distribution of the contents of both the major elements and the impurity elements is zonal in nature, which made it possible to identify the rim, mantle, and core zones in crystals.

The rim zone is characterized by an increased content of Co (0.07–0.09 wt%), for individual crystals of pyrites, increased contents of Ni and Sb are recorded (max C_{Ni} up to 0.28 wt%; max C_{Sb} = up to 0.11 wt%). In the mantle zone, the minimum contents of Cu, Ni, and Pb are observed. The core zone is characterized by an increased content of As (0.98–2.24 wt% at V_σ = 24%), but maximum concentrations are recorded in the rim zone.

Arsenopyrite1 is characterized by a non-stoichiometric composition [(S+As)/Fe≠2.00], an excess of S (C_S = 19.96–23.21 wt%) and the lack of As (C_{As} = 41.81–45.98 wt%) (Figure 6B). Fe content is close to stoichiometric (Me=34.36 wt%). Elements-impurities are Co, Ni, Cu, and Sb (Figure 6C). The constant impurity is Co (V_σ=35%). The distribution of the remaining impurities is very uneven.

6.2 Fluid inclusion analysis

6.2.1 Fluid inclusion petrography

Fluid inclusions were studied in quartz from quartz2 of the main producing arsenopyrite-pyrite-carbonate-quartz vein association. The classification of fluid inclusions into primary and secondary

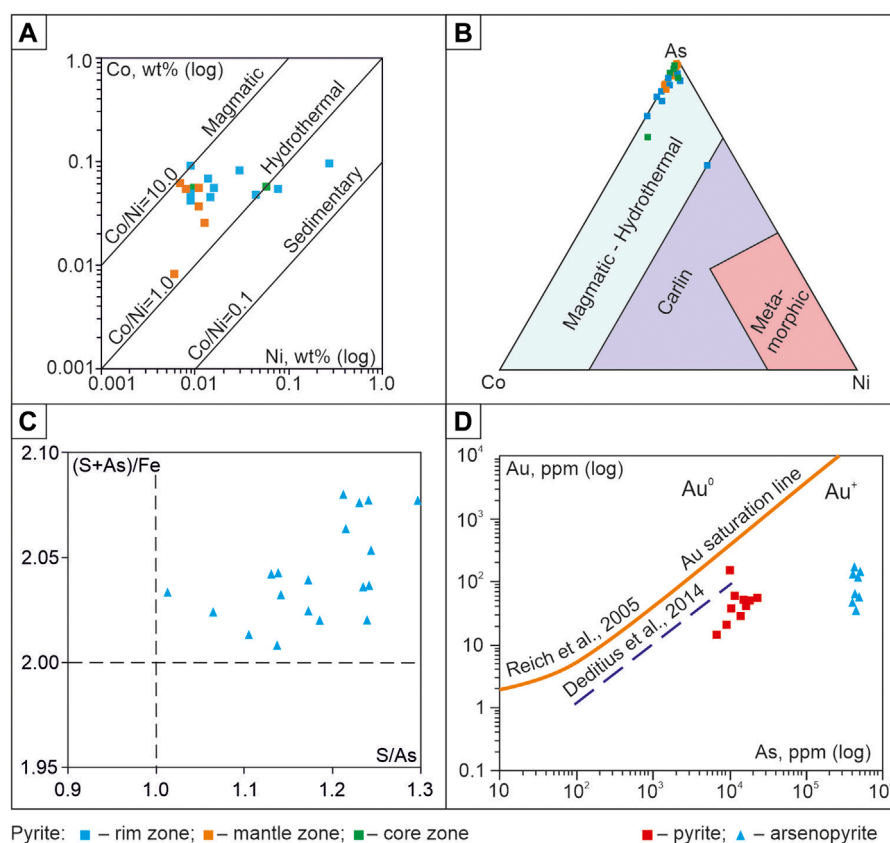


FIGURE 8

(A) Binary plot of Co vs. Ni concentration in pyrites. The demarcated fields are after Xu (1998) and Bajwah et al. (1987); (B) Ternary plot of As-Co-Ni concentration in pyrites. The demarcated fields are after Yan et al. (2012); (C) Binary plot of S/As vs. (S + As)/Fe in proximal alteration arsenopyrite. The intersection of the lines S/As = 1 and (S + As)/Fe = 2 corresponds to the stoichiometric composition (Sazonov et al., 2016); (D) Gold concentration in pyrite and arsenopyrite plotted against As concentration. The Au saturation line is after Reich et al. (2005) and Deditius et al. (2014).

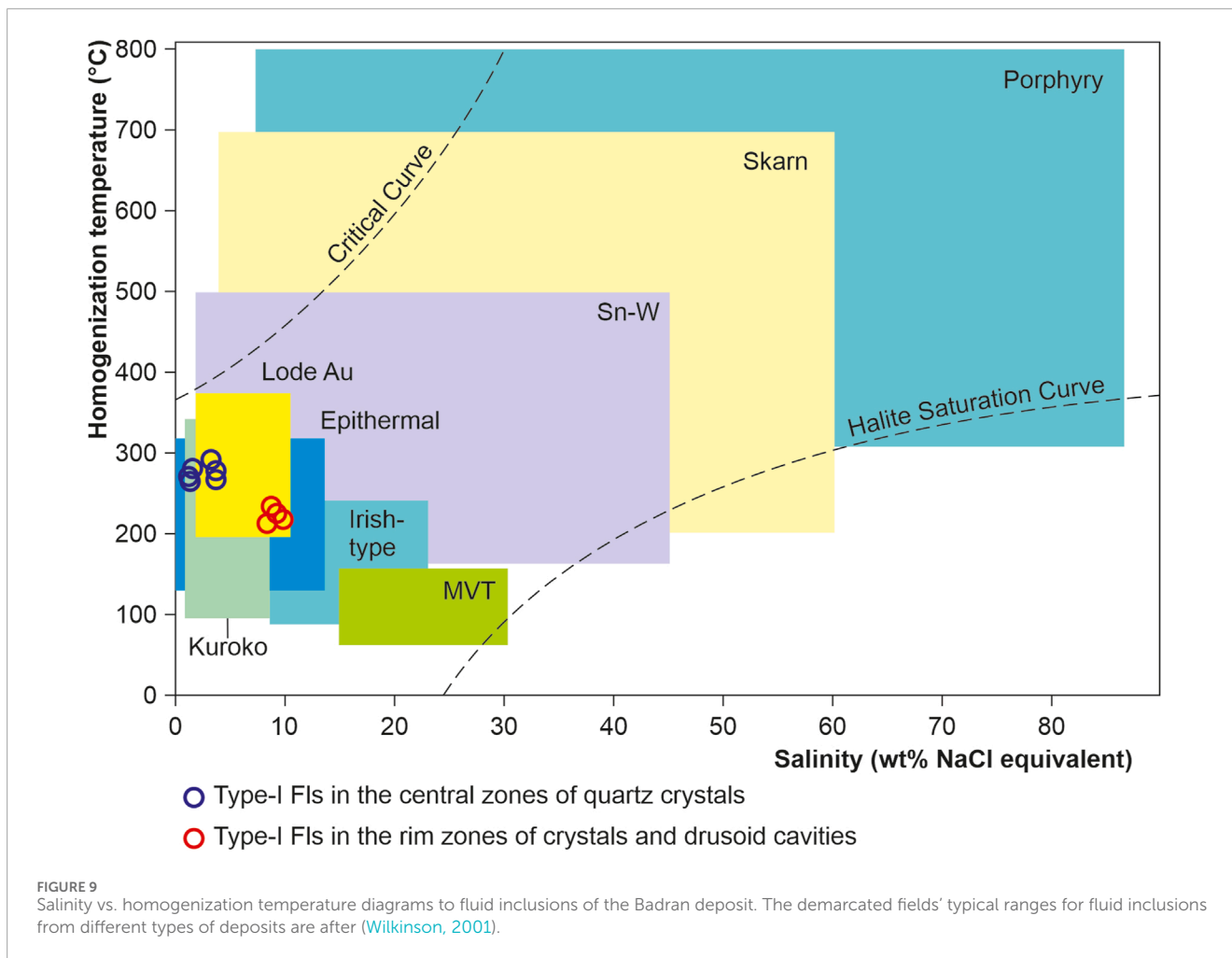
in doubly polished sections was carried out using the criteria described by Roedder (1984). In most of the studied samples, only small and very small gas-liquid inclusions 5–10 μm in size were found (Figure 7). Measurements were carried out only in primary and pseudosecondary inclusions in the central and outer zones of quartz crystals from veins containing visible gold of the main ore-forming stages. Pseudosecondary inclusions are also used for analysis (Yardley and Bodnar, 2014) since they are cogenetic to a later ore event that brought a significant amount of gold into the quartz vein system. Their analysis is important for understanding the evolution of the ore-forming system. Considering the degree of filling, two coexisting types of fluid inclusions (FI) are identified. Type I inclusions are essentially gaseous (65–100 vol% gas), whereas type II inclusions are liquid-gaseous (10–20 vol% gas). The homogenization temperature, pressure, and fluid composition in inclusions from the central (type-IA and type-IIA) and external (type-IB and type-IIB) zones of quartz crystals differ significantly (Table 2).

6.2.2 PTX results of the fluid inclusions study

In the central zones of the crystals, a large number of relatively evenly distributed primary coexisting carbonic-aqueous to aqueous-carbonic types IA and IIA fluid inclusions and their

clusters are observed (Figure 7A). Type IA and IIA inclusions have similar homogenization temperatures, but different salinities (Figure 7D). Homogenization of inclusions occurs in the interval of 265°C–300°C by dissolving carbon dioxide in water (Type IIA) or by evaporation of water (Type IA). Salinities range from 3.2% to 3.6% (Type IIA) to 1.4%–1.6% (Type IA) in wt% NaCl equivalent. When the inclusions are cooled, a gas hydrate is formed, which does not allow accurate measurement of the temperature of the eutectic of the water-salt solution. The first ice melting temperature in inclusions varies from –30 to –25°C, which indicates a predominantly chloride composition of salts (Borisenko, 1977). Thus, the fluid inclusion study shows that the ore fluids have low salinity and are CO₂-rich. Petrography and microthermometric results suggest that fluid immiscibility occurred during the gold mineralization stage. The fluid immiscibility was likely responsible for the deposition of gold and sulfide minerals (Ni et al., 2015).

The outer zones of crystals are composed of water-transparent quartz which contains mainly gas-liquid inclusions (type-IIB) with a small bubble and homogenization temperatures to the liquid phase from 250° to 210°C. The eutectic temperature (the first ice melting) of solutions of inclusions is –7.5...–7.0°C, which indicates a predominantly chloride-bicarbonate-sulfate composition of salts



(Borisenko et al., 2007). The concentration of solutions at the melting point of the last ice crystal is estimated at 8–10 wt% NaCl-eq.

In association with gas-liquid inclusions are low-density gas inclusions (type-IB) (Figure 7B). During cooling in some vacuoles (favorable in shape), freezing of CO₂ and the formation of liquid methane rim is observed (Figure 7C). The mole fraction of methane, determined by the melting and evaporation temperature of carbon dioxide, is 70%–75% (Thiery and al, 1994).

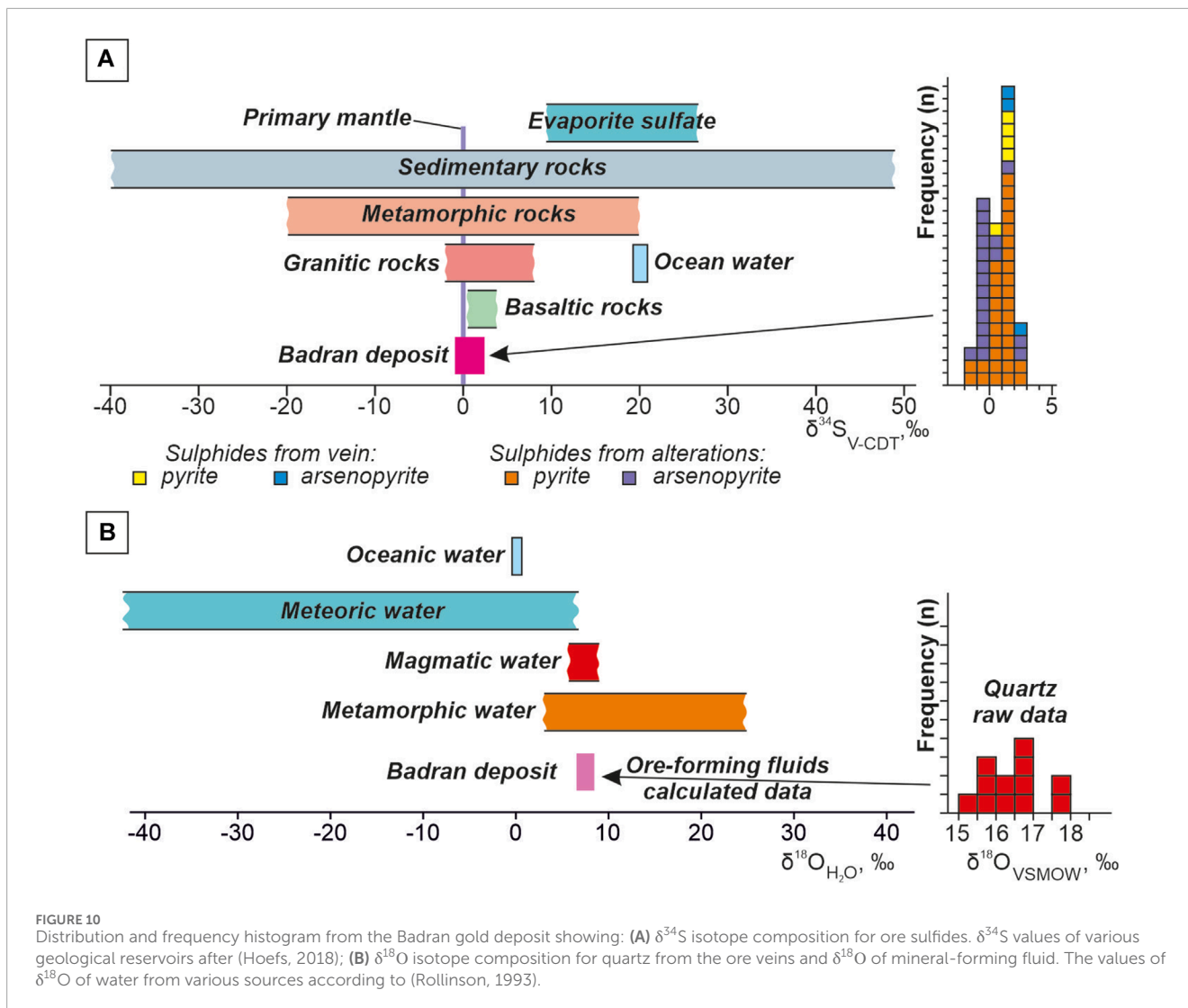
The association of liquid and gas inclusions (Types IB and IIB) suggests that they were also captured simultaneously from a heterogeneous (boiling) fluid. Consequently, the measured homogenization temperatures of the gas-liquid (type-IIB) inclusions correspond to the conditions of their capture.

The presence of coexisting carbonic and aqueous-carbonic inclusions in the same clusters and trails provides evidence for considering them as trapped contemporaneously in the two-phase immiscible field. If so, the trapping pressures for the coexisting types IA+IIA and IB+IIB can be established using trapping temperatures for the high-density type B fluid inclusions and densities for the low-density type A fluid inclusions (e.g., Roedder, 1984).

The melting point of carbon dioxide in inclusions (from –58.5 to –59.6°C) indicates the presence of a significant impurity of

methane (and probably nitrogen) in the fluid. Densities (molar volumes) for the fluid inclusions containing fractions of methane in addition to CO₂ can be determined by the melting point of CO₂ and the homogenization temperature of methane-carbon dioxide fluid using the diagrams from Thiery et al. (1994). The type IB fluid inclusion density is about 330 cm³/mol. Correspondingly, using the computing programs of Bakker (2003), the trapping pressure for type IB+IIB inclusions (trapping temperature 210°C–220°C) is estimated at 125 bar.

The density of the carbonic phase in type IA fluid inclusions is about 180–200 cm³/mol. Taking into account the volume fraction of carbon dioxide (about 65 vol%), the composition and density of the inclusions can be calculated (Roedder, 1984). Calculations indicate that fluids in type IA inclusions contain 85–82 mol% H₂O, 15–18 mol% CO₂ (+CH₄). Their molar volume is about 42–43 cm³/mol (Table 2). Using the computing programs of Bakker (2003), the trapping pressure for type IA+IIA inclusions (trapping temperature 285°C–270°C) is estimated at 250–300 bar. It should be noted that according to experimental data (Figure 7D), the fluid contained in type IIA inclusions could be captured from a homogeneous solution only at pressures above 500 bar.



6.2.3 Bulk composition of fluid inclusions

Bulk analysis makes it possible to estimate the composition of fluid inclusions regardless of their size. The results obtained from 23 samples are given in [Supplementary Table S3](#). According to the predominance of the main fluid components, the samples are divided into several groups, which can be considered as samples containing mainly one or another of the types of fluid inclusions described above (or a combination thereof). Samples containing water-carbon dioxide inclusions (type IA+IIA) are identified by a high concentration of CO_2 , as well as CH_4 and Cl. There is a direct correlation between these components and water. In this group, some samples are recognized separately, in which the chlorine ion content was below the detection limit, despite the large amount of CO_2 . It can be assumed that these samples contain mainly substantially gaseous inclusions (type IA). Quartz with inclusions of low-temperature bicarbonate-sulfate solutions (type IIB) is identified by high SO_4 contents in aqueous extracts. In some samples along with abnormal amounts of sulfate, very high concentrations of Fe, Mn, Ba, Sr, as well as Cu, Zn, and Pb were found. Similar concentrations of elements in extracts may indicate

in favor of their presence in the form of mineral phases (including in the form of daughter minerals in inclusions). It should be noted here that in samples with visible sulfide mineralization, the sulfate ion is not found. As noted above, inclusions that are substantially methane in composition are present in association with inclusions of low-temperature sulfate solutions. However, CH_4 and SO_4 show a negative correlation in bulk analysis. However a significant increase in the CO_2/CH_4 ratio in samples with type-IB+IIB FI indicates that during the analysis, CH_4 and SO_4 react with each other.

6.3 Stable S–O isotope study

The new and previously obtained sulfur isotope results are given in [Table 3](#). The isotopic composition of pyrite and arsenopyrite sulfur from ore veins with visible gold and proximal alteration of the Badran deposit is characterized by a narrow range of values from -1.1‰ to $+2.4\text{‰}$, average value of $+0.4\text{‰}$. $\delta^{34}\text{S}$ values of arsenopyrite from alterations vary from -1.1 to $+2.4\text{‰}$, and of arsenopyrite from quartz veins from $+1.1$ to $+2.3\text{‰}$. *In situ*

TABLE 4 Concentrations of Au (ppm) in pyrite and arsenopyrite from proximal alterations rocks of the Badran deposit.

No	Sample	Rock	Au, ppm
Pyrite3			
1	B-16-19	Alteration rock after siltstones	154.3
2	B-17-19		53.0
3	B-24/1-19		36.9
4	B-26-19		36.7
5	B-28-19		53.1
6	B-33-19		19.6
7	B-35/1-19		155.5
8	B-41-19		13.7
9	B-44-19	Alteration rock after sandstones	62.4
10	B-52-19		33.8
11	B-54/1-19		26.2
12	B-56/1-19		45.4
Arsenopyrite1			
13	B-24/2-19	Alteration rock after siltstones	123.6
14	B-35/2-19		34.8
15	B-54/2-19	Alteration rock after sandstones	52.3
16	B-56/2-20		56.9

determination of $\delta^{34}\text{S}$ in arsenopyrite from alterations showed its homogeneous isotopic composition. Variations in the magnitude of $\delta^{34}\text{S}$ in pyrites from the proximal alteration vary from -0.7 to $+2.1\text{‰}$ (mean $\sim +0.9\text{‰}$, coefficient of variation $\text{CV} = 80\%$), which is somewhat wider than in pyrite from quartz veins from $+1.0$ to $+1.4\text{‰}$.

According to the values of $\delta^{34}\text{S}$ in pyrite, two types of crystals are identified from the proximal alteration (Fridovsky et al., 2022). The first type is isotopically inhomogeneous with sulfur weighting from the center to the periphery of the grains (the average in the center of the grains is $+0.2\text{‰}$, average at the periphery of the grains is $+1.5\text{‰}$). The difference in the value of $\delta^{34}\text{S}$ is up to 2.1‰ . The second type, taking into account the analysis error, is isotopically homogeneous pyrite, in which the values of $\delta^{34}\text{S}$ in the center of crystals do not significantly (0.0‰ – 0.3‰) differ from the periphery.

The $\delta^{18}\text{O}$ values of quartz from ore veins with visible gold of the Badran deposit, selected at various depth levels, vary in a narrow range from $+15.1$ to $+17.5\text{‰}$ (mean $+16.4\text{‰}$, $n = 12$). The oxygen isotopic composition of the water included in these fluids is calculated considering the entrapment temperatures of primary inclusions in quartz (290°C – 210°C) and equilibrium constants for oxygen isotope exchange between quartz and water (Clayton et al.,

1972). The range of $\delta^{18}\text{O}_{\text{H}_2\text{O}}$ values was quite uniform ($+7.5\text{‰} \pm 1\text{‰}$).

7 Discussion

7.1 Genesis of pyrite and arsenopyrite and gold endowment

The analysis of the Co, Ni, and As content in pyrite and As, S, and Fe in arsenopyrite and the ratios of these elements is important for determining the conditions of formation and genesis of these minerals with invisible gold in Badran deposit (Bralia et al., 1979; Bajwah et al., 1987; Azovskova et al., 2014; Reich et al., 2016; Roman et al., 2019; Large and Maslennikov, 2020).

The Co/Ni ratio in pyrite varies from 0.3 to 9.9, which is typical for p-type pyrite with high conductivity. Such negatively charged pyrite according to data (Large and Maslennikov, 2020) mainly attracts gold. For most of the analyzed grains, $\text{Co}/\text{Ni} > 1$, which according to (Zhang et al., 2014; Roman et al., 2019) is characteristic of hydrothermal fluids (Figure 8A). Considering the As-Co-Ni system, it is possible to judge the conditions of pyrite formation. Co and Ni are of mantle origin, but Ni is a part of the minerals already at the early stages of magmatic melt migration. The Co content is quite stable in the hydrothermal fluid. As passes into the solid phase at lower temperatures, isomorphically replacing S in pyrite. In the As-Co-Ni diagram (Figure 8B), the points are concentrated at the top of As, which may indicate, as mentioned earlier when discussing the results of the study of fluid inclusions, the formation of pyrite at a shallow depth from solutions of combined composition.

Variations of As and S contents even within one grain in the metasomatic arsenopyrite of the Badran deposit amount to 0.6–1.2 wt%. The constant excess of S with a lack of As and the high “mobility” of these elements in solution leads to a violation of the mineral structure and distortion of the octahedral environment of Fe atoms (Sazonov et al., 2016). The graph (Figure 8C) demonstrates the non-stoichiometric composition of Aspy ($\text{S}/\text{As} = 1.01$ – 1.30 ; $(\text{S}+\text{As})/\text{Fe} = 2.01$ – 2.08), which reflects the instability of the ore formation regime.

Pyrite3 and arsenopyrite1 are the main gold-bearing minerals in the proximal alteration of the Badran deposit. Gold can be either in the form of isomorphic substitution of Fe, As, and S in these minerals of non-stoichiometric composition or in the form of microinclusions. Microinclusions of native gold were not observed in the studied sulfides, but their gold content is high (in pyrite up to 155.5 ppm Au and in arsenopyrite up to 123.6 ppm Au) (Table 4). The position of Au concentrations in Py and Apy below the saturation line is characteristic of the structurally related form of “invisible” Au^+ gold (Figure 8D). This type of gold content is described in many gold deposits of various ages (Reich et al., 2005; Deditius et al., 2014). Non-stoichiometry of the compositions and imperfection of the structure of pyrite and arsenopyrite provides wide possibilities for isomorphic substitution of Au^+ mineral-forming elements (As, Fe, S) (Figure 8D).

7.2 The origin of fluids in the evolution of the ore-forming system

Based on the results of the study of fluid inclusions from quartz veins with visible gold of the Badran deposit, its formation was determined at temperatures from 290°C to 210°C and pressures from 250 to 125 bar. The obtained temperatures correspond to orogenic gold deposits in the western part of the YKMB, but the pressure is lower (Fridovsky et al., 2020). Mineral formation at the Badran deposit occurred under conditions of heterogenization (boiling) of ore-bearing fluids and the change of the lithostatic pressure gradient by hydrostatic one. In the process of ore formation, the composition of gold-bearing solutions has significantly evolved. Early pyrite-arsenopyrite metasomatic and arsenopyrite-pyrite-carbonate-quartz vein mineral associations were formed with the involvement of diluted alkaline-chloride methane-carbon dioxide fluids ($C=1.5\text{--}3.5$ wt% NaCl-eq., $x_{\text{CO}_2+\text{CH}_4} = 4\text{--}6$ mol%, $\text{CO}_2/\text{CH}_4 = 5\text{--}7$). The late polymetallic-carbonate-albite-quartz and sulfostibnite-sericite-quartz mineral associations were deposited after a drop in temperature and pressure from sulfur-methane solutions ($C = 8\text{--}10$ wt% NaCl eq., $x_{\text{CO}_2+\text{CH}_4} < 1$ mol%, $\text{CO}_2/\text{CH}_4 = 0.3\text{--}0.4$). The obtained parameters are typical for the Phanerozoic orogenic deposits (Wilkinson, 2001; Goldfarb and Groves, 2015). In low- and moderately-saline fluids, the sulfide (HS^-) complex can be the major agent for gold transportation in hydrothermal fluids in the Badran gold deposit (Monsef and Abdelnasser, 2021). The change from the early stages to the late stages of the P-T parameters of the ore fluid, its cooling, pressure reduction, and interaction with surrounding rocks leads to a decrease in the solubility of gold, destabilization of $\text{Au}(\text{HS})_2$, gold precipitation in association with sulfides Fe, Pb, Zn, and Cu.

Studied fluid inclusions (type-I, -II) from quartz veins with visible gold of the Badran deposit at discrimination diagram of Wilkinson (2001) of salinity vs. homogenization temperature they fall, mostly to the field of vein Au deposits (Figure 9). The above suggests the origin of ore-bearing fluids in the Badran area from various sources of deep metamorphic reservoirs and subcrustal lithospheric mantle (SCLM). The latter was fertilized in the time preceding mineralization (Late Jurassic) and was derived directly from the down-going subduction slab and overlying sediment wedge at the closure of the Oymyakon Ocean according to the model (Groves et al., 2020).

7.3 Source of metals and ore fluids

Sulfur and oxygen isotope data provide an opportunity to gain useful information about possible sources of metals and ore fluids (Wilkinson, 2001). Studies of the isotopic composition of sulfur pyrite ($\delta^{34}\text{S}$ from -0.7 to $+2.1$ ‰) and arsenopyrite ($\delta^{34}\text{S}$ from -1.1 to $+2.4$ ‰) of the Badran deposit have shown that $\delta^{34}\text{S}$ are close to sulfides from gold-quartz veins of orogenic deposits in the western part of the YKMB (arsenopyrite—from -2.1 to $+2.4$ ‰, pyrite—from -6.6 to $+5.4$ ‰ (Gamyranin et al., 2018; Kudrin et al., 2021; Fridovsky et al., 2022) and are characterized by a smaller range of variations than $\delta^{34}\text{S}$ in pyrite from quartz veins and alterations (mean $+4.0$ ‰) of the Upper-Kolyma gold-bearing area

(Tyukova and Voroshin, 2008). Similar isotopic composition of sulfur arsenopyrite and pyrite of orogenic OGDs of the western part of the YKMB and disseminated mineralization from ore alterations of the Badran deposit indicates their formation during a single isotope equilibrium evolving hydrothermal event under conditions of phase separation of ore-forming fluids.

According to the data (Hoefs, 2018), various ore-forming sources are characterized by individual values of $\delta^{34}\text{S}$ of sulfides (Figure 10A). Sulfur from marine environments shows $\delta^{34}\text{S}$ values of $\sim +20$ ‰, wide variations in the value of $\delta^{34}\text{S}$ are determined for sedimentary (from -40 ‰ to $+50$ ‰) and metamorphic (from -20 ‰ to $+20$ ‰) reservoirs. The isotopic composition $\delta^{34}\text{S}$ of sulfur from granite is estimated by (from -2 ‰ to $+10$ ‰), basalt—from 0 ‰ to $+5$ ‰). The values of $\delta^{34}\text{S}$ close to zero are characteristic of mantle or mantle-derived sources. The average isotopic composition of sulfur pyrite and arsenopyrite from alterations and ore veins of the Badran deposit is close to 0 ‰ (Figure 10A) and is consistent with the data obtained from other OGD of the western part of the YKMB (Fridovsky et al., 2013; Fridovsky et al., 2014; Fridovsky et al., 2015; Gamyranin et al., 2018; Kudrin et al., 2021; Fridovsky et al., 2022).

Values of $\delta^{34}\text{S}$ close to 0 ‰ show that the sulfur is consistent with fluids of subcontinental lithospheric mantle and magmatic origin. The obtained results may indicate the involvement of a deep source of sulfur in ore formation at the Badran deposit. The combination of the narrow $\delta^{34}\text{S}$ range and the lack of sharp change from the depth of 600 m to the surface the fluid temperature and salinity showed that ore-forming fluids and sources were stable. Such conditions can be an essential requirement for large-scale gold mineralization (Li et al., 2023).

Isotopic composition of oxygen quartz from ore veins with native gold of the Badran deposit (from $+15.1$ to $+17.5$ ‰) is somewhat narrower than the range characteristic of gold-quartz deposits in the western part of the YKMB (from $+14.2$ to $+19.5$ ‰ (Gamyranin et al., 2018)), is close to $\delta^{18}\text{O}$ quartz of the super-large Nezhdaninskoe gold deposit (from $+14.8$ to $+16.6$ ‰ (Bortnikov et al., 2007)), but it is somewhat heavier than for the Natalka deposit (from $+11.6$ to $+14.1$ ‰ (Goryachev et al., 2008)) (Figure 10B). The obtained values of $\delta^{18}\text{O}$ quartz are comparable to the Phanerozoic orogenic gold deposits (from $+12$ up to $+18$ ‰ (Kerrick, 1990; Ridley and Diamond, 2000). The close values of $\delta^{18}\text{O}$ quartz from different sites of the Badran deposit may indicate a homogeneous source of fluids of the deep metamorphic thermal system.

The oxygen isotopic composition of the water included in these fluids is calculated considering the entrapment temperatures of primary inclusions in quartz ($290^\circ\text{C}\text{--}210^\circ\text{C}$) and equilibrium constants for oxygen isotope exchange between quartz and water (Figure 10B) (Clayton et al., 1972). The obtained relatively uniform range of $\delta^{18}\text{O}_{\text{H}_2\text{O}}$ values ($+7.5$ ‰ \pm 1‰) indicates a probable paragenetic relationship of ore-forming fluids with magmas or metamorphic reservoirs (Rollinson, 1993).

Thus, the obtained results of studying fluid systems, S-O stable isotopes, and geochemistry of sulfides from proximal alteration confirm that the ore-forming fluids of the Badran deposit did not have a single origin, but were obtained from a mixture of subcontinental lithospheric mantle and metamorphic sources.

8 Conclusion

- 1) The Badran polychronous gold deposit contains typically orogenic disseminated mineralization with arsenian pyrite and arsenopyrite ores with invisible gold, quartz veins with native gold and sulfides Fe, Pb, Zn, Cu, and sulfosalts, as well as locally post-ore minerals Ag, Sb, and Hg epithermal features. It was formed in six stages of mineralization: (I) metasomatic pyrite-arsenopyrite, (II) arsenopyrite-pyrite-carbonate-quartz, (III) polymetal-carbonate-albite-quartz, (IV) sulfostibnite-sericite-quartz, (V) silver-quartz, (VI) cinnabar-stibnite-carbonate-quartz. The sericite-chlorite-carbonate-quartz proximal alteration contains the disseminated arsenian pyrite and arsenopyrite with high contents of invisible structurally bound Au⁺. Disseminated and vein ores are controlled by thrust structures, which are transit routes for trans-crustal fluids.
- 2) Ore formation at the Badran gold deposit occurred under conditions of heterogenization (boiling) of low-saline aqueous-carbonic fluids. At an early stage, the fluids had an alkaline-chloride methane-carbon dioxide composition. At a late stage, with a drop in temperature and pressure, they contained sulfur-methane solutions. The change of the P-T parameters of the ore-forming fluid, boiling and the interaction with the surrounding rocks led to a decrease in solubility and precipitation of gold.
- 3) The combination of the narrow $\delta^{34}\text{S}$ range and the lack of sharp change with the depth of the fluid temperature and salinity showed that ore-forming fluids and sources were stable. Such conditions can be an essential requirement for large-scale gold mineralization.
- 4) The results obtained confirm that the ore-forming fluids of the Badran gold deposit did not have a single origin, but were obtained from a mixture of subcontinental lithospheric mantle and metamorphic sources.

Data availability statement

The original contributions presented in the study are included in the article/[Supplementary Material](#), further inquiries can be directed to the corresponding author.

Author contributions

VF: Conceptualization, Data curation, Formal Analysis, Funding acquisition, Investigation, Methodology, Project administration, Supervision, Validation, Writing–original draft, Writing–review and editing. SK: Conceptualization, Formal

Analysis, Investigation, Methodology, Validation, Writing–original draft, Writing–review and editing. LP: Conceptualization, Formal Analysis, Methodology, Writing–original draft, Writing–review and editing. MK: Conceptualization, Formal Analysis, Methodology, Validation, Visualization, Writing–original draft, Writing–review and editing. GA: Conceptualization, Formal Analysis, Methodology, Validation, Writing–original draft, Writing–review and editing.

Funding

The author(s) declare financial support was received for the research, authorship, and/or publication of this article. This research was financially supported by the Diamond and Precious Metals Geology Institute, Siberian Branch of the Russian Academy of Sciences (FUG-2024-0006). Isotope geochemical studies was supported by the Russian Science Foundation (RSF) (project no. 23-47-00064).

Acknowledgments

The authors would like to thank some reviewers for their thorough reviews which have greatly improved the manuscript.

Conflict of interest

The authors declare that the research was conducted in the absence of any commercial or financial relationships that could be construed as a potential conflict of interest.

Publisher's note

All claims expressed in this article are solely those of the authors and do not necessarily represent those of their affiliated organizations, or those of the publisher, the editors and the reviewers. Any product that may be evaluated in this article, or claim that may be made by its manufacturer, is not guaranteed or endorsed by the publisher.

Supplementary material

The Supplementary Material for this article can be found online at: <https://www.frontiersin.org/articles/10.3389/feart.2024.1340112/full#supplementary-material>

References

- Akinin, V. V., Prokopiev, A. V., Toro, J., Miller, E. L., Wooden, J., Goryachev, N. A., et al. (2009). U–Pb SHRIMP ages of granitoids from the Main batholith belt (North East Asia). *Dokl. Earth Sci.* 426, 216–221. doi:10.1134/S1028334X09040217
- Amuzinsky, V. A. (2005). *Metallogenic epochs and content of ore complexes of the Verkhoyansk folded system*. Yakutsk: YSU Publishing House. (In Russian).
- Anisimova, G. S., Amuzinsky, V. A., and Balandin, V. A. (1998). Sulfide-quartz deposits in gently sloping faults – a new type of gold deposits. *Russ. Geol.* 6, 65–70. (In Russian).
- Anisimova, G. S., Kondratieva, L. A., Serkebaeva, E. S., and Ageenko, V. A. (2008). Badran gold deposit, eastern yakutia. *Ores Metals* 5, 49–60. (In Russian).

- Azovskova, O. B., Utochkina, N. V., and Zubova, T. P. (2014). *Geochemical features of pyrite and marcasite from weathering crusts and "ancient" loose deposits of the Aktai area (Northern Urals)* in *Ezhgodnik-2013, Tr. IGG UrO RAN*. Ufa, Russia: URO RAN, 238–245. (In Russian).
- Bajwah, Z. U., Seccombe, P. K., and Offler, R. (1987). Trace element distribution, Co:Ni ratios and genesis of the Big Cadia iron-copper deposit, New South Wales, Australia. *Min. Deposita* 22, 292–303. doi:10.1007/bf00204522
- Bakker, R. J. (2003). Package FLUIDS 1. Computer programs for analysis of fluid inclusion data and for modelling bulk fluid properties. *Chem. Geol.* 194, 3–23. doi:10.1016/S0009-2541(02)00268-1
- Bodnar, R. J., and Vityk, M. O. (1994). *Interpretation of microthermometric data for H₂O-NaCl fluid inclusions*. Blacksburg, Virginia Tech, 117–130.
- Borisenko, A. S. (1977). Cryometric study of salt composition of solutions in gas-liquid inclusions in minerals. *Geol. Geofiz.* 8, 16–28. (In Russian).
- Bortnikov, N. S., Vikent'eva, O. V., Prokof'ev, V. Yu., Gamyaniin, G. N., Alpatov, V. A., and Bakharev, A. G. (2007). Fluid composition and origin in the hydrothermal system of the Nezhdaninsky gold deposit, Sakha (Yakutia), Russia. *Geol. Ore Dep.* 49 (2), 87–128. doi:10.1134/S1075701507020018
- Bralia, A., Sabatini, G., and Troja, F. (1979). A reevaluation of the Co/Ni ratio in pyrite as geochemical tool in ore genesis problems. *Min. Depos.* 14, 353–374. doi:10.1007/bf00206365
- Clayton, R. N., O'Neil, J. R., and Mayeda, T. K. (1972). Oxygen isotope exchange between quartz and water. *J. Geophys. Res.* 77, 3057–3067. doi:10.1029/jb077i017p03057
- Darling, R. S. (1991). An extended equation to calculate NaCl contents from final clathrate melting temperatures in H₂O-CO₂-NaCl fluid inclusions: implications for PT-isochors location. *Geoch. Cosmochim. Acta* 55, 3869–3871. doi:10.1016/0016-7037(91)90079-k
- Deditius, A. P., Reich, M., Kesler, S. E., Utsunomiya, S., Chryssoulis, S. L., Walshe, J., et al. (2014). The coupled geochemistry of Au and as in pyrite from hydrothermal ore deposits. *Geoch. Cosmochim. Acta* 140, 644–670. doi:10.1016/j.gca.2014.05.045
- Fridovsky, V. Y. (1999). Strike slip fault duplexes of the Badran deposit (North-East Yakutia). *Izvestiya vysshikh uchebnykh zavedenii. Geol. Explor.* 1, 60–66. (In Russian).
- Fridovsky, V. Y. (2002). "Structures of gold ore fields and deposits of the Yana-Kolyma ore belt." *Metallogeny of collisional geodynamic settings*. Editors N. V. Mezhelevsky, and G. S. Gusev (Moscow: GEOS), 1, 6–241. (In Russian).
- Fridovsky, V. Y. (2018). Structural control of orogenic gold deposits of the Verkhoyansk-Kolyma folded region, northeast Russia. *Ore Geol. Rev.* 103, 38–55. doi:10.1016/j.oregeorev.2017.01.006
- Fridovsky, V. Y., Gamyaniin, G. N., and Polufuntikova, L. I. (2013). The Sana Au-quartz deposit within the Taryn ore cluster. *Razvedka Okhrana Nedr* 2, 3–7. (In Russian).
- Fridovsky, V. Y., Gamyaniin, G. N., and Polufuntikova, L. I. (2014). Gold-quartz and antimony mineralization in the Maltan deposit in Northeast Russia. *Russ. J. Pac Geol.* 8 (4), 276–287. doi:10.1134/S1819714014040034
- Fridovsky, V. Y., Gamyaniin, G. N., and Polufuntikova, L. I. (2015). Structures, mineralogy, and fluid regime of ore formation in the polygenetic Malo-Taryn gold field, Northeast Russia. *Russ. J. Pac Geol.* 9 (4), 274–286. doi:10.1134/S1819714015040028
- Fridovsky, V. Y., Goryachev, N. A., Krymsky, R. S., Kudrin, M. V., Belyatsky, B. V., and Sergeev, S. A. (2021). The Age of gold mineralization in the Yana-Kolyma metallogenic belt, Northeastern Russia: first data of Re-Os isotope geochronology of native gold. *Russ. J. Pac. Geol.* 15 (4), 293–306. doi:10.1134/S1819714021040035
- Fridovsky, V. Y., Kudrin, M. V., Polufuntikova, L. I., and Goryachev, N. A. (2017). Ore-controlling thrust faults at the Bazovskoe gold-ore deposit (Eastern Yakutia). *Dokl. Earth Sci.* 474 (2), 617–619. doi:10.1134/S1028334X17060034
- Fridovsky, V. Y., Polufuntikova, L. I., Gamyaniin, G. N., and Solovyov, E. E. (2015). Orogenic gold deposits with significant resource potential in the central part of the Yana-Kolyma belt. *Explor. Prot. Min. res* 11, 3–9. (In Russian).
- Fridovsky, V. Y., Polufuntikova, L. I., Kudrin, M. V., and Goryachev, N. A. (2022). Sulfur isotope composition and geochemical characteristics of gold-bearing sulfides of the Badran orogenic deposit, Yana-Kolyma metallogenic belt (North-East Asia). *Dokl. Earth Sci.* 502 (1), 3–9. doi:10.1134/S1028334X22010032
- Fridovsky, V. Y., Vernikovskaya, A. E., Yakovleva, K. Y., Rodionov, N. V., Travin, A. V., Matushkin, N. Y., et al. (2022). Geodynamic formation conditions and age of granitoids from small intrusions in the west of the Yana-Kolyma gold belt (Northeast Asia). *Russ. Geol. Geophys* 63 (4), 483–502. doi:10.2113/RGG20214442
- Fridovsky, V. Y., Yakovleva, K. Y., Vernikovskaya, A. E., Rodionov, N. V., Vernikovskiy, V. A., Matushkin, N. Y., et al. (2020). Geodynamic emplacement setting of the Late Jfrassic dikes of the Yana-Kolyma gold belt, NE folded framing of the Siberian craton: geochemical, petrologic, and U-Pb zircon data. *Minerals* 10 (11), 1–27. doi:10.3390/min10111000
- Fridovsky, V. Y., Yakovleva, K. Y., Vernikovskaya, A. E., Vernikovskiy, V. A., Rodionov, N. V., and Lokhov, K. I. (2020). Late jurrassic (151–147 Ma) dike magmatism of the northeastern margin of the siberian craton. *Dokl. Earth Sci.* 491 (1), 117–120. doi:10.1134/S1028334X2003006X
- Fu, J., Hu, Z., Li, J., Yang, L., Zhang, W., Liu, Y., et al. (2017). Accurate determination of sulfur isotopes ($\delta^{33}\text{S}$ and $\delta^{34}\text{S}$) in sulfides and elemental sulfur by femtosecond laser ablation MC-ICP-MS with non-matrix matched calibration. *J. Anal. At. Spectrom.* 32, 2341–2351. doi:10.1039/C7JA00282C
- Gamyaniin, G. N., Fridovsky, V. Y., and Vikent'eva, O. V. (2018). Noble-metal mineralization of the Adycha-Taryn metallogenic zone: geochemistry of stable isotopes, fluid regime, and ore formation conditions. *Russ. Geol Geoph* 59 (10), 1271–1287. doi:10.1016/j.rgg.2018.09.006
- Gertseva, M. V., Luchitskaya, M. V., Sysoev, I. V., and Sokolov, S. D. (2021). Stages of formation of the main batholith belt in the Northeast of Russia: U-Th-Pb SIMS and Ar-Ar geochronological data. *Dokl. Akad. Nauk.* 499 (1), 5–10. doi:10.31857/S2686739721070057
- Goldfarb, R., and Groves, D. (2015). Orogenic gold: common or evolving fluid and metal sources through time. *Lithos* 233, 2–26. doi:10.1016/j.lithos.2015.07.011
- Goldfarb, R. J., Taylor, R., Collins, G., Goryachev, N. A., and Orlandini, O. F. (2014). Phanerozoic continental growth and gold metallogeny of Asia. *Gondwana Res.* 25 (1), 48–102. doi:10.1016/j.gr.2013.03.002
- Goryachev, N. A., and Pirajno, F. (2014). Gold deposits and gold metallogeny of Far East Russia. *Ore Geol. Rev.* 59, 123–151. doi:10.1016/j.oregeorev.2013.11.010
- Goryachev, N. A., Vikentyeva, O. V., Bortnikov, N. S., Prokofiev, V. Y., Alpatov, V. A., and Golub, V. V. (2008). World-class Natalka gold deposit: REE distribution, fluid inclusions, stable oxygen isotopes and ore formation conditions (North-East of Russia). *Geol. Rudn. Mest.* 50, 414–444. (In Russian).
- Groves, D. I., Santosh, M., Deng, J., Wang, Q. F., Yang, L. Q., and Zhang, L. (2020). A holistic model for the origin of orogenic gold deposits and its implications for exploration. *Min. Depos.* 55, 275–292. doi:10.1007/s00126-019-00877-5
- Ignatiev, A. V., Velivetskaya, T. A., Budnitskiy, S. Y., Yakovenko, V. V., Vysotskiy, S. V., and Levitskii, V. I. (2018). Precision analysis of multisulfur isotopes in sulfides by femtosecond laser ablation GC-IRMS at high spatial resolution. *Chem. Geol.* 493, 316–326. doi:10.1016/j.chemgeo.2018.06.006
- Kerrick, R. (1990). Mesothermal gold deposits: a critique of genetic hypotheses. Greenstone gold and crustal evolution, in Greenstone gold and crustal evolution. *NUNA Conf. Volume*, 13–31.
- Kesler, S. E. (2005). Ore-forming fluids. *Elements* 1 (1), 13–18. doi:10.2113/gselements.1.1.13
- Khanchuk, A. I. (2006). In *Geodynamics, magmatism and metallogeny of the East of Russia*. Editor A. I. Khanchuk (Vladivostok: Dalnauka). (In Russian).
- Konstantinov, M. M. (2010). *Gold deposits of Russia*. Moscow: Akvarel. (In Russian).
- Kryazhev, S. G., Prokofiev, V. Y., and Vasyuta, Y. V. (2006). *The use of the ICP MS method in the analysis of the composition of ore-forming fluids of hydrothermal ore deposits*. *Vestnik of the Moscow University* (4), 30–36. (In Russian).
- Kudrin, M. V., Fridovsky, V. Y., Polufuntikova, L. I., and Kryuchkova, L. Y. (2021). Disseminated gold-sulfide mineralization in metasomatites of the khangalas deposit, yana-kolyma metallogenic belt (northeast Russia): analysis of the texture, geochemistry, and S isotopic composition of pyrite and arsenopyrite. *Minerals* 11, 403. doi:10.3390/min11040403
- Large, R. R., and Maslennikov, V. V. (2020). Invisible gold paragenesis and geochemistry in pyrite from orogenic and sediment-hosted gold deposits. *Minerals* 10, 339. doi:10.3390/min10040339
- Liu, Z., Ni, P., Zhang, Y.-Q., Sheng, Z.-L., Wang, G.-G., Zhang, S.-L., et al. (2021). An Early Cretaceous gold metallogenesis in the Wuhe area, Eastern Anhui province: constraints from geology, fluid inclusion, H-O isotope and geochronology on the Hekou gold deposit. *Ore Geol. Rev.* 138, 104319. doi:10.1016/j.oregeorev.2021.104319
- Monsef, M., and Abdelnasser, A. (2021). Ore-forming mechanism and its relationship with deformational and metamorphic episodes at Haimur gold mine, Nubian Shield, Egypt. *Geol. Mag.* 158 (3), 518–536. doi:10.1017/S0016756820000655
- Neustroev, R. G. (2003). Conditions of localization of ore pillars of the Badran deposit (Yakutia). *Izvestiya vuzov. Geol. Explor* 3, 54–57. (In Russian).
- Ni, P., Wang, G. G., Chen, H., Xu, Y. F., Guan, S. J., Pan, J. Y., et al. (2015). An early paleozoic orogenic gold belt along the Jiang-Shao fault, south China: evidence from fluid inclusions and Rb-Sr dating of quartz in the huangshan and pingshui deposits. *J. Asian Earth Sci.* 103, 87–102. doi:10.1016/j.jseas.2014.11.031
- Obolensky, A. A., Gushchina, L. V., Anisimova, G. S., Serkebaeva, E. S., Tomilenko, A. A., and Gibsher, N. A. (2011). Physicochemical modeling of mineral formation processes at the Badran gold deposit (Yakutia). *Russ Geol Geoph* 52, 290–306. doi:10.1016/j.rgg.2011.02.003
- Parfenov, L. M., and Kuzmin, M. I. (2001). "Tectonics," in *Geodynamics and metallogeny of the territory of the republic of sakha (yakutia)*. Editors L. M. Parfenov, and M. I. Kuzmin (Moscow: Nauka/Interperiodika). (In Russian).
- Prokopiev, A. V., Borisenko, A. S., Gamyaniin, G. N., Pavlova, G. G., Fridovsky, V. Y., Kondrat'eva, L. A., et al. (2018). Age constraints and tectonic settings of metallogenic and magmatic events in the Verkhoyansk-Kolyma folded area. *Russ Geol Geoph* 59 (10), 1237–1253. doi:10.1016/j.rgg.2018.09.004

- Protopopov, G. H., Truschelev, A. M., and Kuznetsov, Y. V. (2019). State geological map of the Russian federation scale 1:1000 000 third generation. Verkhoyansk-kolymsk series. Sheet Q-54 – ust-nera. *Explanatory note. Ministry of natural resources of Russia, rosnedra, FSBI VSEGEI, JSC yakutskgeologiya*. St. Petersburg: VSEGEI Publishing House. 845.
- Reich, M., Kesler, S. E., Utsunomiya, S., Palenik, C. S., Chryssoulis, S. L., and Ewing, R. C. (2005). Solubility of gold in arsenian pyrite. *Geochim. Cosmochim. Acta* 69, 2781–2796. doi:10.1016/j.gca.2005.01.011
- Reich, M., Simon, A., Deditius, A., Barra, F., Chryssoulis, S., Lagas, G., et al. (2016). Trace element signature of pyrite from the los colorados iron oxide-apatite (IOA) deposit, Chile: a missing link between andean IOA and iron oxide copper-gold systems. *Econ. Geol.* 111, 743–761. doi:10.2113/econgeo.111.3.743
- Ridley, J. R., and Diamond, L. W. (2000). Fluid chemistry of orogenic lode gold deposits and implication for genetic models. *Gold 2000 Rev. Econ. Geol.* 13, 141–162. doi:10.5382/Rev.13.04
- Roedder, E. (1984). “Fluid inclusions,” in *Reviews in mineralogy*. Editor H. P. Ribbe (Washington DC: Mineralogical Society of America), 12, 1–644.
- Roman, N., Reich, M., Leisen, M., Morata, D., Barra, F., and Deditius, A. P. (2019). Geochemical and micro-textural fingerprints of boiling in pyrite. *Geochim Cosmochim Acta* 246, 60–85. doi:10.1016/j.gca.2018.11.034
- Sazonov, A. M., Kirik, S. D., Silyanov, S. A., Bayukov, Y. A., and Tishin, P. A. (2016). Typomorphism of arsenopyrite of the blagodatnoye and olympiada gold deposits (yenisei ridge). *Mineralogy* 3, 53–70. (in Russian) <https://elibrary.ru/wzvrof>.
- Sharp, Z. D. (1990). A laser-based microanalytical method for the *in situ* determination of oxygen isotope ratios of silicates and oxides. *Geochim. Cosmochim. Acta* 54, 1353–1357. doi:10.1016/0016-7037(90)90160-m
- Soloviev, S. G., Kryazhev, S. G., Dvurechenskaya, S. S., Vasyukov, V. E., Shumilin, D. A., and Voskresensky, K. I. (2019). The superlarge Malmyzh porphyry Cu-Au deposit, Sikhote-Alin, eastern Russia: igneous geochemistry, hydrothermal alteration, mineralization, and fluid inclusion characteristics. *Ore Geol. Rev.* 113, 103112. doi:10.1016/j.oregeorev.2019.103112
- Tan, B., Ni, P., Li, S.-N., Xiang, H.-L., Wang, G.-G., Chi, Z., et al. (2020). Geological, fluid inclusion, and H–O–C–S–Pb isotopic constraints on the genesis of the Shuangqishan gold deposit, Fujian, China. *J. Geochem. Explor.* 214, 106544. doi:10.1016/j.gexplo.2020.106544
- Thiery, R., Kerkhof, A. M., and Dubessy, J. (1994). vX properties of CH₄-CO₂ and CO₂-N₂ fluid inclusions: modeling for T < 31 °C and P < 400 bars. *Eur. J. Mineral.* 6, 753–771.
- Toro, J., Miller, E. L., Prokopyev, A. V., Zhang, X., and Veselovskiy, R. (2016). Mesozoic orogens of the arctic from novaya zemlya to Alaska. *J. Geol. Soc.* 173 (6), 989–1006. doi:10.1144/jgs2016-083
- Tyukova, E. E., and Voroshin, S. V. (2008). Isotopic composition of sulfur in sulfides from ores and host rocks of the Upper Kolyma region (Magadan region). *Russ. J. Pac. Geol.* 27, 29–43. doi:10.1007/s11720-008-1003-y
- Valley, J. W., Kitchen, N., Kohn, M. J., Niendorf, C. R., and Spicuzza, M. J. (1995). UWG-2, a garnet standard for oxygen isotope ratios: strategies for high precision and accuracy with laser heating. *Geochim. Cosmochim. Acta.* 59, 5223–5231. doi:10.1016/0016-7037(95)00386-x
- Velivetskaya, T. A., Ignatiev, A. V., Yakovenko, V. V., and Vysotskiy, S. V. (2019). An improved femtosecond laser-ablation fluorination method for measurements of sulfur isotopic anomalies ($\delta^{33}\text{S}$ and $\delta^{36}\text{S}$) in sulfides with high precision. *Rapid Commun. Mass Spectrom.* 33, 1722–1729. doi:10.1002/rcm.8528
- Vikenteva, O. V., Prokofiev, V. Y., Gamyagin, G. N., Bortnikov, N. S., and Goryachev, N. A. (2018). Intrusion-related gold-bismuth deposits of North-East Russia: PTX parameters and sources of hydrothermal fluids. *Ore Geol. Rev.* 102, 240–259. doi:10.1016/j.oregeorev.2018.09.004
- Warr, L. N. (2021). IMA-CNMNC approved mineral symbols. *Mineral. Mag.* 85 (3), 1–30. doi:10.1180/mgm.2021.43
- Wilkinson, J. (2001). Fluid inclusions in hydrothermal ore deposits. *Lithos* 55, 229–272. doi:10.1016/S0024-4937(00)00047-5
- Yang, L., Wang, Q., Groves, D. I., Lu, S. L., Huajian, W. P., Peng, W., et al. (2021). Multiple orogenic gold mineralization events in a collisional orogen: insights from an extruded terrane along the southeastern margin of the Tibetan Plateau. *J. Struct. Geol.* 147, 104333. doi:10.1016/j.jsg.2021.104333
- Yardley, B. W. D., and Bodnar, R. J. (2014). Fluids in the continental crust. *Geochem. Perspect.* 3 (1), 1–127. doi:10.7185/geochempersp.3.1
- Zaitsev, A. I., Fridovsky, V. Y., Vernikovskaya, A. E., Kudrin, M. V., Yakovleva, K. Y., and Kadilnikov, P. I. (2018). Rb-Sr isotopic study of basites of the Tarynsky dike complex of the ore-magmatic system (North-East of Russia). *Russ. Geol.* 5, 50–61.
- Zhang, W., Wang, C., Wei, X., Fan, M., and Chen, L. (2014). The implications and typomorphic characteristics of pyrite chemical composition in zijinshan gold-copper deposit[J]. *Adv. Earth Sci.* 29(8): 974–984. doi:10.11867/j.issn.1001-8166.2014.08.0974